




Transport signatures of single and multiple Floquet Majorana modes in one-dimensional Rashba nanowire and Shiba chain

Debashish Mondal ^{1,2,*}, Rekha Kumari,^{3,†} Tanay Nag ^{4,‡} and Arijit Saha ^{1,2,§}

¹*Institute of Physics, Sachivalaya Marg, Bhubaneswar-751005, India*

²*Homi Bhabha National Institute, Training School Complex, Anushakti Nagar, Mumbai 400094, India*

³*International Centre for Theoretical Sciences, Tata Institute of Fundamental Research, Bengaluru 560 089, India*

⁴*Department of Physics, BITS Pilani-Hyderabad Campus, Telangana, 500078, India*

We theoretically investigate the transport signature of single and multiple Floquet Majorana end modes (FMEMs), appearing in an experimentally feasible setup with Rashba nanowire (NW) placed in closed proximity to a conventional s -wave superconductor, in the presence of an external Zeeman field. Periodic drive causes the anomalous π -modes to emerge in addition to the regular 0-modes in the driven system where the former does not exhibit any static analog. For single 0- and/or π -FMEM, differential conductance exhibits a quantized value of $2e^2/h$ while we consider the sum over all the photon sectors, supporting Floquet sum rule. We examine the stability of this summed conductance against random onsite disorder. We further investigate the summed conductance in several cases hosting multiple (more than one) 0- or π -modes at the end of the NW. In these cases, we obtain quantized values of $n \times 2e^2/h$ of summed conductance with n being the number of modes (0 / π) located at one end of NW. We repeat our analysis for another experimentally realizable model system known as helical Shiba chain. Moreover, we corroborate our results by computing the differential conductance for FMEMs using non-equilibrium Green's function method. Our work opens up the possibility of studying the transport signatures of FMEMs in these realistic models.

I. INTRODUCTION

In recent times, Majorana fermions (MFs) in the form of Majorana zero modes (MZMs) associated with topological superconductor [1–6] have received enormous attention due to their non-Abelian braiding properties. This suffices them to serve as the fundamental unit for topological quantum computations [7–11]. Initially, Kitaev introduced the concept of MZMs in his seminal theoretical paper, proposing their existence at the ends of a one-dimensional (1D) spinless p -wave superconducting chain [1]. However, the inherent challenge of accessing p -wave superconductivity has hindered the experimental realization of Kitaev's proposal. Nevertheless, an experimentally viable configuration involving a 1D Rashba nanowire (NW) in close proximity to a regular s -wave superconductor under the influence of an external Zeeman field could effectively emulate a 1D p -wave superconductor [3–5, 12–15]. Based on semiconducting NW-superconductor heterostructure, zero bias peak in differential conductance has been observed in various transport experiments which manifest the indirect signatures of the MZMs [14–19]. In this direction, there exists an alternative approach based on helical spin chain [20–33] in which magnetic adatoms are implanted on the surface of a bulk s -wave superconductor [34–41]. Here, MZMs appear within the minigap of emergent Shiba bands. The existence of MZMs in such setup has been experimentally verified via several recent experiments [42–50] using

scanning tunneling microscopy (STM) measurements.

In current literature, Floquet engineering represents an efficient and advanced route for tailoring desired topology in a non-topological system [51–74]. The intricate winding of the time-dependent wave function results in the inception of anomalous topological boundary modes at finite quasi-energy, termed as π -modes leaving no static equivalence. Emergence of multiple Floquet Majorana end modes (FMEMs) has been explored in p -wave Kitaev chain [62–64], 1D cold-atomic NW- s -wave superconductor heterostructure [65, 67–70], realistic 1D Rashba NW-superconductor hybrid setup [75] and also in helical Shiba chain model [76]. The possibility of braiding these out of equilibrium Floquet modes further gives rise to significant future research avenues in the direction of topological quantum computations [77–80].

In this direction, the transport signature of FMEMs was first explored in 1D Kitaev model by executing Floquet sum rule to obtain quantized $2e^2/h$ peak for summed conductance $\tilde{\sigma}$ [81]. The robustness of the quantized peaks against disorder was also emphasized. In the presence of periodic driving, the concept of the Floquet sum rule is inspected to other setups such as quantum well heterostructure (a two-dimensional (2D) quantum spin Hall insulator) [82] and topological insulator [83] leading to non-quantized value ($< 2e^2/h$ or $> 2e^2/h$) of summed differential conductance $\tilde{\sigma}$ at zero bias. In this case, it has been shown that the zero bias peak (ZBP) $< 2e^2/h$ values to be robust against disorder while others $> 2e^2/h$ are not. Further investigation in this direction leads to a planner Josephson junction with proximitized heterostructure based on 2D electron gas with Rashba spin-orbit coupling (SOC) and Zeeman field [69]. However, the transport signatures of FMEMs, appearing in an experimentally realizable Rashba NW model

* debashish.m@iopb.res.in

† rekha.kumari@icts.res.in

‡ tanay.nag@physics.uu.se

§ arijit@iopb.res.in

and helical Shiba chain model, are yet to be explored to the best of our knowledge. This motivates us to examine the transport signatures of dynamical Majorana modes once their number can be tuned. At first, we generalize the theory of Floquet transport for FMEMs [81] considering the systems possessing spin/chiral degrees of freedom (DOF). Then the intriguing questions that we address here are the following: How do Floquet sidebands contribute to the quantized signal of differential conductance in such Rashba NW-parent s -wave superconductor hybrid setup? How can we understand the relation between the stability and quantization of regular and anomalous Majorana modes in the presence of disorder? What is the role of the bulk gap associated with FMEMs as far as the stability of quantized differential conductance against disorder is concerned? How does the differential conductance behave when multiple FMEMs are localized at one end of the concerned system?

In this article, first, we begin with the experimentally feasible 1D Rashba NW model in close proximity of a bulk s -wave superconductor (see Fig. 1 for our schematic setup). The heterostructure manifests itself as an effective p -wave superconductor by hosting a pair of MZMs at the ends of the NW in the topological regime. For completeness, we study the transport property of these static zero-energy MEMs. We demonstrate the differential conductance σ_{stat} as a function of bias voltage V where we obtain the quantized ZBP value of $2e^2/h$ for σ_{stat} at $V = 0$ (see Fig. 2) as an indirect signature of MZMs. To investigate the transport signature of FMEMs, we apply three-step periodic drive protocol that results in regular 0- and anomalous π -FMEMs in the system [75]. We calculate one-terminal differential conductance σ for individual photon sectors, their sum $\tilde{\sigma}$ and represent them as a function of bias voltage V for four cases where single 0- and/or π -modes are located at one end of the NW. For all these cases, we encounter quantized values of $\tilde{\sigma}$ corresponding to 0- and π -modes. However, the individual photon sector does not yield quantized response unless the Floquet sum rule over all the photon sectors is satisfied [81] (see Fig. 4). We check the robustness of $\tilde{\sigma}$ against random onsite disorder for all the above instances, (see Fig. 5). We also explore the cases when multiple (more than one) 0- and/or π -modes are present at one end of the NW (see Fig. 6). We extend our investigation to another practically realizable model based on magnetic adatoms on the surface of an s -wave superconductor namely, helical Shiba chain model, and obtain qualitatively identical results akin to the previous model (see Fig. 7 for schematic representation and Fig. 8 for the results). After a complete study of the transport signature of FMEMs for both the realistic models, we adopt another numerical approach based on non-equilibrium Green's function (NEGF) method to validate our results further. We also provide possible experimental feasibility of our theoretical findings.

The remaining parts of our article are arranged as fol-

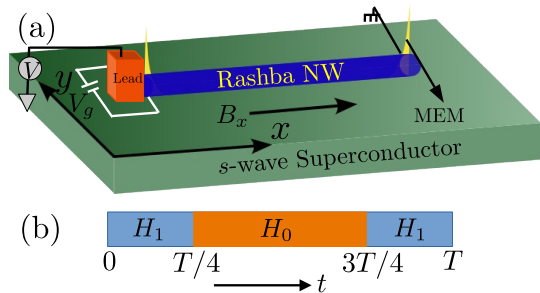


FIG. 1. (a) Schematic diagram of our setup is presented to study transport signature of FMEMs in Rashba nanowire (NW) model. Here, a one-dimensional NW (blue) with strong Rashba spin-orbit coupling is placed on top of a common s -wave superconducting substrate (green) in the presence of an external magnetic field B_x applied along the length of the NW (x -direction). A pair of MZMs (yellow) emerges at the ends of the NW. To tune the chemical potential a gate voltage V_g is applied to the NW. A metallic lead (orange) is attached to one end of the NW and a bias voltage V is applied across the lead to measure single terminal differential conductance while another end of the NW is connected to the ground. (b) Three-step drive protocol, according to Eq. (2), is schematically depicted here to generate FMEMs.

lows. We introduce the static Hamiltonian for Rashba NW model in Sec. II A and demonstrate the drive protocol to engineer FMEMs in Sec. II B. In Sec. III A, we briefly review the Floquet theory needed to examine the differential conductance. We briefly discuss the transport theory for Floquet and static MEMs in Secs. III B and III C, respectively. We discuss the transport results for static Rashba NW in Sec. IV A for completeness. In case of driven Rashba NW, we illustrate our results for single FMEM in Sec. IV B and their stability against disorder in Sec. IV C. In Sec. IV D, we present the same for multiple FMEMs. Sec. V is devoted to the transport study of static and Floquet MEMs in case of helical Shiba chain model. We present our results using NEGF technique in Sec. VI. The choice of parameters for our numerical findings and the corresponding experimental feasibility of our setups are described in Sec. VII. Finally, we summarise and conclude in Sec. VIII.

II. MODEL AND DRIVING PROTOCOL

A. Model Hamiltonian

We consider a 1D Rashba NW placed on the top of an s -wave superconductor in presence of a Zeeman field applied parallel to the NW [3, 4, 12, 13, 75]. Superconductivity is induced in the NW as a consequence of the proximity effect. Let us consider the Bogoliubov-de Gennes (BdG) basis: $\Psi_j = \{\psi_{j\uparrow}, \psi_{j\downarrow}, \psi_{j\downarrow}^\dagger, -\psi_{j\uparrow}^\dagger\}^t$ with $\psi_{j\uparrow}^\dagger$ ($\psi_{j\uparrow}$)

and $\psi_{j\downarrow}^\dagger$ ($\psi_{j\downarrow}$) stand for the creation (annihilation) operator at j^{th} site for spin-up and spin-down sectors, respectively, while \mathbf{t} represents the transpose operation. Then BdG Hamiltonian for this setup can be written as [75]

$$H_0 = \sum_{j=1}^N \Psi_j^\dagger [(2t_h - c_0)\Gamma_1 + B_x\Gamma_3 + \Delta\Gamma_4] \Psi_j + \sum_{j=1}^{N-1} \Psi_{j+1}^\dagger [-t_h\Gamma_1 - iu\Gamma_2] \Psi_j + H.c., \quad (1)$$

where, the 4×4 - Γ -matrices are given by $\Gamma_1 = \tau_z\sigma_0$, $\Gamma_2 = \tau_z\sigma_z$, $\Gamma_3 = \tau_0\sigma_x$, and $\Gamma_4 = \tau_x\sigma_0$ with the Pauli matrices $\boldsymbol{\tau}$ and $\boldsymbol{\sigma}$ act on particle-hole and spin subspaces, respectively. Here c_0 , t_h , B_x , u , and Δ denote chemical potential, nearest neighbour hopping amplitude, magnetic field, Rashba SOC strength and proximity induced s -wave superconductor gap inside the NW, respectively. This system exhibits topological phase boundaries given by $\sqrt{c_0^2 + \Delta^2} \leq |B_x| \leq \sqrt{(4t_h - c_0)^2 + \Delta^2}$ [75]. In the topological regime, under open boundary condition (OBC), the NW hosts one Majorana 0-mode at each of its ends [75].

B. Driving protocol

In order to Floquet band engineering of our system, we consider the following 3-step periodic drive protocol reads as

$$\begin{aligned} H(t) &= H_1 = \sum_{j=1}^N \Psi_j^\dagger [-c_1\Gamma_1] \Psi_j \quad t \in \left[0, \frac{T}{4}\right), \\ &= H_0 \quad t \in \left[\frac{T}{4}, \frac{3T}{4}\right), \\ &= H_1 = \sum_{j=1}^N \Psi_j^\dagger [-c_1\Gamma_1] \Psi_j \quad t \in \left[\frac{3T}{4}, T\right), \end{aligned} \quad (2)$$

where, H_1 term denotes the modulation of the onsite chemical potential only and T ($=2\pi/\Omega$) is the time period of the drive. Starting from the non-topological regime of the static Hamiltonian [Eq.(1)] we can generate regular Floquet 0- and anomalous π -modes appearing in our system due to the application of the above mentioned drive [Eq.(2)]. By changing the frequency Ω and amplitude c_1 of the drive, one can also achieve control over the number of these emergent FMEMs [75].

III. FLOQUET TRANSPORT THEORY

In this section, we briefly discuss the Floquet theory for investigating the transport properties of FMEMs and static MZMs. However, the details are discussed in Appendix A, Appendix B and Appendix C.

A. Floquet theory

For a periodically driven system i.e., $H(t+T) = H(t)$, following the analogy with Bloch theorem, the solution of the Schrödinger's equation $H(t)|\psi_{\bar{\alpha}}(t)\rangle = i\partial_t|\psi_{\bar{\alpha}}(t)\rangle$ takes the form $|\psi_{\bar{\alpha}}(t)\rangle = e^{-i\epsilon_{\bar{\alpha}}t}|u_{\bar{\alpha}}(t)\rangle$ with $|u_{\bar{\alpha}}(t)\rangle = |u_{\bar{\alpha}}(t+T)\rangle$. Here, $|u_{\bar{\alpha}}(t)\rangle$ coined as Floquet states are the eigenvectors of effective Hamiltonian $H_{\text{eff}} = H(t) - i\partial_t$, $H_{\text{eff}}|u_{\bar{\alpha}}(t)\rangle = \epsilon_{\bar{\alpha}}|u_{\bar{\alpha}}(t)\rangle$ and corresponding eigenvalues $\epsilon_{\bar{\alpha}}$ are called the quasi-energies [84, 85]. With the help of the periodicity of $|\psi(t)\rangle$, the time evolution operator $U(T, 0)$ satisfies the following relation: $U(T, 0)|u_{\bar{\alpha}}(T)\rangle = e^{-i\epsilon_{\bar{\alpha}}T}|u_{\bar{\alpha}}(T)\rangle$. From the eigenvalues $\Lambda_{\bar{\alpha}}$ of $U(T, 0)$, we compute quasi-energies $\epsilon_{\bar{\alpha}} = (i/T)\ln(\Lambda_{\bar{\alpha}})$. $\epsilon_{\bar{\alpha}} \rightarrow \epsilon_{\bar{\alpha}} + n\Omega$ with $n \in \mathbb{Z}$ provides a new set of $\{|u_{\bar{\alpha}}(t)\rangle\} \rightarrow \{e^{in\Omega t}|u_{\bar{\alpha}}(t)\rangle\}$ for the same set of $\{|\psi_{\bar{\alpha}}(t)\rangle\}$. Consequently, the quasi-energies are not unique and are connected via the periodic drive by the absorption and emission of virtual photons. As a result, these frequency indices are commonly referred to as photon indices (side bands) within the context of Floquet theory [81, 84]. Nonetheless, quasi-energies maintain uniqueness within the realm of the first Floquet zone or the 0th photon sector: $-\Omega/2 \leq \epsilon_{\bar{\alpha}} \leq \Omega/2$. Fourier decomposition of the periodic $|u_{\bar{\alpha}}(t)\rangle$ is given by $|u_{\bar{\alpha}}(t)\rangle = \sum_n e^{-in\Omega t}|u_{\bar{\alpha}}^{(n)}\rangle$ and related frequency space Schrödinger's equation takes the form: $[H^{(k-n)} - k\Omega]|u_{\bar{\alpha}}^{(n)}\rangle = \epsilon_{\bar{\alpha}}|u_{\bar{\alpha}}^{(k)}\rangle$ with $H^{(k-n)} = \int_0^T \frac{dt}{T} e^{i(k-n)\Omega t} H(t)$. Note that, $|u_{\bar{\alpha}}^{(k)}\rangle$ constitute a Hilbert space called extended Hilbert space (see Appendix D) where expectation value of an observable \mathcal{O} is defined as $\langle\langle\mathcal{O}\rangle\rangle = \sum_k \langle u_{\bar{\alpha}}^{(k)} | \mathcal{O} | u_{\bar{\alpha}}^{(k)} \rangle$ [81]. See Appendix B for more details.

B. Transport theory of Floquet Majorana modes

For transport study of FMEMs, we consider the setup as mentioned in Fig. 1. One end of the system (Rashba NW) is connected to a single channel metallic lead attached to a thermal reservoir. We apply bias voltage via this lead and another end of the NW is connected to the ground. Here, we assume that the lead follows the Fermi-Dirac distribution function and does not change with time indicating the lead density of states ρ to be constant. The attached lead introduces an imaginary self-energy $\delta_{\bar{\alpha}}$ to the quasi-energy $\epsilon_{\bar{\alpha}}$ of the driven system. For bias voltage V , one terminal (single lead) differential conductance is given by (see Appendix C for detailed discussion)

$$\sigma(V) = -2\pi e^2 \int d\omega \sum_k \text{Tr} \left[\mathbf{G}^{(k)\dagger}(\omega) \mathbf{V}^t \mathbf{G}^{(k)}(\omega) \mathbf{V} \right] f'(\omega), \quad (3)$$

where f represents the Fermi-Dirac distribution function, and $G^{(k)}$ is the Nambu-Gorkov Green's function given

by [69]

$$\mathbf{G}^{(k)}(\omega) = \sum_{\bar{\alpha}, n} \frac{|u_{\bar{\alpha}}^{(k+n)}\rangle\langle u_{\bar{\alpha}}^{(n)}|}{\omega - \epsilon_{\bar{\alpha}} - n\Omega + i\delta_{\bar{\alpha}}}. \quad (4)$$

We define the coupling parameter $\nu = 2\pi\rho t_h^2$. In the weak coupling limit ($\nu \ll t_h$), the \mathbf{V} matrix, carrying the information of coupling between the lead and system, vanishes everywhere except for the contact site i.e., $\mathbf{V} = \mathbf{V}^c \oplus 0 \oplus 0 \oplus 0 \dots$, with \mathbf{V}^c is given by

$$\mathbf{V}^c = \rho t_h^2 \frac{1}{2} \begin{pmatrix} 1 & i \\ -i & 1 \end{pmatrix} \otimes \begin{pmatrix} 1 & 0 \\ 0 & 1 \end{pmatrix}. \quad (5)$$

Here, \mathbf{V} is a $4N \times 4N$ diagonal matrix out of which all the remaining $N - 1$ blocks are null matrix except for the first block designated by \mathbf{V}^c . In this limit Eq. (3) reduces to

$$\sigma(V) = -\frac{e^2\nu^2}{2\pi} \times 2 \times \sum_{k, s, s'} \int d\omega |G_{he, ss'}^{c(k)}(\omega)|^2 f'(\omega), \quad (6)$$

where $G_{he, ss'}^{c(k)}$ is the hole (with s -spin/chirality)-electron (with s' -spin/chirality) component of Nambu-Gorkov Green's function for photon sector k computed at the contact site. Moreover, weak coupling approximation between the system and lead motivates one to perform perturbative analysis to obtain the self-energy as [81]:

$$\begin{aligned} \delta_{\bar{\alpha}} &= -\langle\langle -\pi(\mathbf{V} + \mathbf{V}^T) \rangle\rangle \\ &= \frac{\nu}{2} \sum_{k, s} \left[|u_{\bar{\alpha}, s}^{c(k)}|^2 + |v_{\bar{\alpha}, s}^{c(k)}|^2 \right], \end{aligned} \quad (7)$$

where $u_{\bar{\alpha}, s}^{c(k)}$, and $v_{\bar{\alpha}, s}^{c(k)}$ denote the particle and hole contribution of the wave function, respectively, for spin/chiral sector s and photon sector k at the contact site. Hence, in the zero temperature limit, the one terminal differential conductance in presence of a bias voltage V is given by

$$\begin{aligned} \tilde{\sigma}(V) &= \lim_{V \rightarrow \epsilon_{\bar{\alpha}}} \frac{e^2\nu^2}{2\pi} \times 2 \sum_{k, s, s'} |G_{he, ss'}^{c(k)}(V + n\Omega)|^2 \\ &\approx \sum_n \frac{2e^2}{h} \sum_{\bar{\alpha}, k, s, s'} \frac{\nu^2}{\delta_{\bar{\alpha}}^2} \times |v_{\bar{\alpha}, s}^{c(k+n)} u_{\bar{\alpha}, s'}^{c(n)}|^2 \times \text{L}\left(\frac{V - \epsilon_{\bar{\alpha}}}{\delta_{\bar{\alpha}}}\right) \\ &= \sum_n \sigma(V + n\Omega), \end{aligned} \quad (8)$$

with contribution from n^{th} photon sector $\sigma(V + n\Omega) = \frac{2e^2}{h} \sum_{\bar{\alpha}, k, s, s'} \frac{\nu^2}{\delta_{\bar{\alpha}}^2} \times |v_{\bar{\alpha}, s}^{c(k+n)} u_{\bar{\alpha}, s'}^{c(n)}|^2 \times \text{L}\left(\frac{V - \epsilon_{\bar{\alpha}}}{\delta_{\bar{\alpha}}}\right) \equiv \sigma^{(n)}(V)$. Here, the Lorentzian is defined by $\text{L}(z) = \frac{1}{1+z^2}$.

C. Transport through static Majorana modes in Rashba NW system

In order to calculate the transport signature of static MZMs, one can follow the above framework considering

a static system. However, there exists a simple way to obtain the corresponding expression by considering the zero amplitude and zero frequency limit of the drive for the driven case. Thus, self-energy for the corresponding static system is given by

$$\delta_{\bar{\alpha}} = \frac{\nu}{2} \sum_s \left[|u_{\bar{\alpha}, s}^c|^2 + |v_{\bar{\alpha}, s}^c|^2 \right]. \quad (9)$$

Then, the expression for one terminal differential conductance, caused by the static MZMs, is given by

$$\sigma_{\text{stat}}(V) = \frac{2e^2}{h} \sum_{\bar{\alpha}, s, s'} \frac{\nu^2}{\delta_{\bar{\alpha}}^2} |v_{\bar{\alpha}, s}^c u_{\bar{\alpha}, s'}^c|^2 \times \text{L}\left(\frac{V - E_{\bar{\alpha}}}{\delta_{\bar{\alpha}}}\right). \quad (10)$$

Here, $E_{\bar{\alpha}}$ denotes the $\bar{\alpha}^{\text{th}}$ eigenvalue of the static Hamiltonian. To be precise, we obtain Eq. (9) from Eq. (7) by excluding the frequency sum k . To obtain Eq. (10) from Eq. (8) we repeat the same and replace quasi-energy $\epsilon_{\bar{\alpha}}$ with static energy eigenvalues $E_{\bar{\alpha}}$.

IV. RESULTS FOR RASHBA NW SETUP

A. Transport signature of static MZMs

To study the transport signature of static MZMs, we begin with topological regime of the static NW Hamiltonian in Eq. (1) hosting one MZM at each of its end (see the probability density $|\Psi|^2$ corresponding to MZMs in Fig. 2). We compute single-terminal differential conductance σ_{stat} using Eq. (10) and show with respect to the bias voltage V (see the inset in Fig. 2). We obtain several small peaks outside the bulk gap in addition to a large peak existing at $V = 0$, called the ZBP. The latter one exhibits a quantized value of $2e^2/h$ as a signature of MZMs, while formers do not show any such universal feature [81]. Here, we consider a large enough system size ($N = 300$) such that wave functions corresponding to two MZMs have no spatial overlap and their single-ended localization profile is ensured. To be precise, one MZM is localized at one end while the remaining MZM is localized at another end of the system. Hence, only one MZM wave function contributes to one terminal differential conductance σ_{stat} leading to the quantized value of $2e^2/h$ at $V = 0$. However, for small system sizes, wave functions corresponding to two MZMs can contribute equally to the σ_{stat} due to their double-ended spatial localization profile. Such overlap in their wave-functions on a given site eventually results in a doubling of the quantized value i.e., $2 \times 2e^2/h$ at $V = 0$ (see Appendix E for details).

B. Transport signature of single 0- and/or π -FMEMs present at one end of the NW

To explore transport signature of FMEMs, we apply step drive protocol as mentioned in Eq. (2) to the

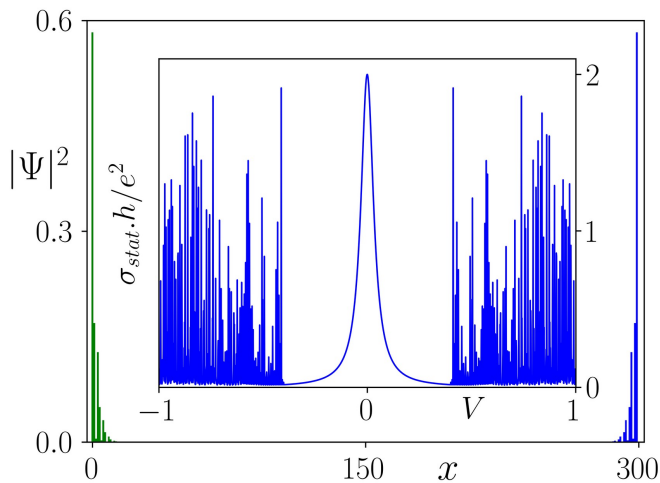


FIG. 2. Probability density $|\Psi|^2$ is depicted as a function of system size corresponding to two static MZMs in case of Rashba NW setup. It is evident that both the wave functions of the static MZMs are localized at two different ends of the NW. The inset features single-terminal differential conductance σ_{stat} calculated from Eq. (10) for the same system. The zero bias ($V=0$) peak of σ_{stat} exhibits a quantized value of $2e^2/h$. We choose system size of $N = 300$ lattice sites and $B_x = 2.0$ for the topological regime. All the other model parameters are chosen as $(c_0, t_h, u, \Delta) = (1.0, 1.0, 0.5, 1.0)$. We consider $\nu = \pi/25$ throughout our manuscript.

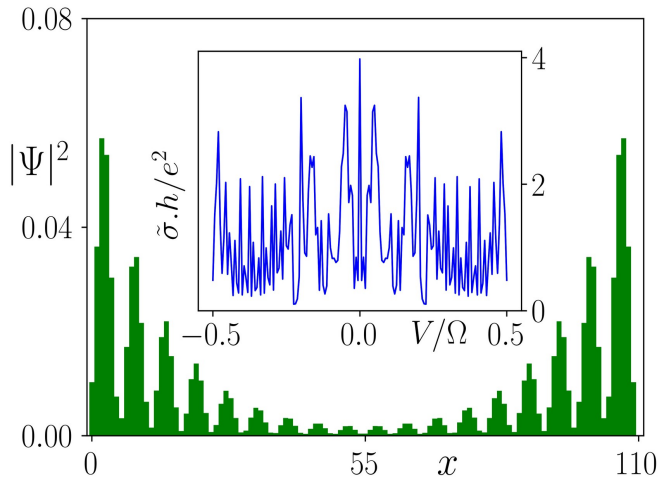


FIG. 3. We illustrate the spatial localization profile of $|\Psi|^2$ for total two 0-energy FMEMs with system size $N = 110$ lattice sites. They spatially overlap with each other. They exhibit equal contributions in conductance arising from the two ends of the NW. In the inset, we demonstrate the summed conductance $\tilde{\sigma}$, calculated from Eq. (8), for the present case. Both of them individually carries the same quantized value of $2e^2/h$ at bias voltage $V = 0$ and thus we obtain $4e^2/h$ quantization for $\tilde{\sigma}$ at $V = 0$. We consider $(c_0, c_1, \Omega, B_x) = (0.25, 0.25, 2.25, 1)$ and all the other model parameters are chosen to be same as mentioned in Fig. 2.

Rashba NW setup. The driven system hosts emergent FMEMs [75]. Here, it is worth mentioning the nomenclature for FMEMs: if the driven system hosts total one pair of Majorana modes with quasi-energy 0 ($\Omega/2$), we label them single 0- (π)-mode. If the system size is large enough, their wave functions do not have any spatial overlap, and one end of the NW hosts only one mode in the above pair for a particular quasi-energy. However, for small system sizes the spatial overlap may take place, but we still keep the same nomenclature. Here, we consider four cases on the basis of number of FMEMs belong to particular quasi-energy, located at one end of the NW and their corresponding bulk gap structure. Case 1: only one 0-mode, case 2: only one π -mode, case 3: one 0- and one π -mode with larger bulk gap for 0-mode as compared to the π -mode, case 4: same as case 3 with larger bulk gap of π -mode than the 0-mode. Note that, Ref. [75] contains rich phase diagram for number of emergent FMEMs in driven Rashba NW setup. Following this, we consider only four representative cases out of many cases to explain the main physical outcome. To compute $\tilde{\sigma}$, we examine Floquet states in frequency space $|u_{\tilde{\alpha}}^{(n)}\rangle$. We obtain these states by diagonalizing the extended space Hamiltonian truncated up to $n = \pm 10$ photon index (see Appendix D for details). To proceed further, we here specify the computational limitations of our analysis: we deal with $84N \times 84N$ dimensional matrix each and every time step (see Appendix D). With the help of the computational facility we have, at best we can go up to $N = 600$ lattice sites. Even at this large system size limit, wave functions for FMEMs may or may not be edge-resolved. Furthermore, for disordered case (see next section for details) we cannot continue with such a large system size. Hence, to have consistency in our results for FMEMs in all cases, we continue our analysis with a moderate system size ($N = 100$ and around that) where the wave functions have spatial overlap on a given edge. (see the probability distribution $|\Psi|^2$ of 0-FMEMs in Fig. 3 for case 1). We compute $\tilde{\sigma}$ for case 1 and depict it as a function of bias voltage V in the inset of Fig. 3. Two FMEMs contribute equally to $\tilde{\sigma}$ for each value of V and especially exhibits quantized value of $2e^2/h$ at $V = 0$ leading to the total quantization of $\tilde{\sigma} = 4e^2/h$. Thus, when l number of Floquet Majorana modes overlap on the contact site, the summed differential conductance takes the value $\tilde{\sigma} = l \times 2e^2/h$. Since, we do not consider large enough system sizes for the driven system, we obtain twice the expected quantized value of $\tilde{\sigma}$. However, in Appendix F we show that for single π -mode we can have edge-resolved wave functions with large enough system sizes where the transport signal is quantized with the value of $2e^2/h$.

For all the four cases mentioned above, we compute one-terminal differential conductance σ for individual photon sectors, and their sum $\tilde{\sigma}$ using Eq. (8). We illustrate them in four panels of Fig. 4. In Fig. 4(a) we represent σ for case 1 with single 0-mode. It is evident that no photon sector exhibits a quantized peak for bias

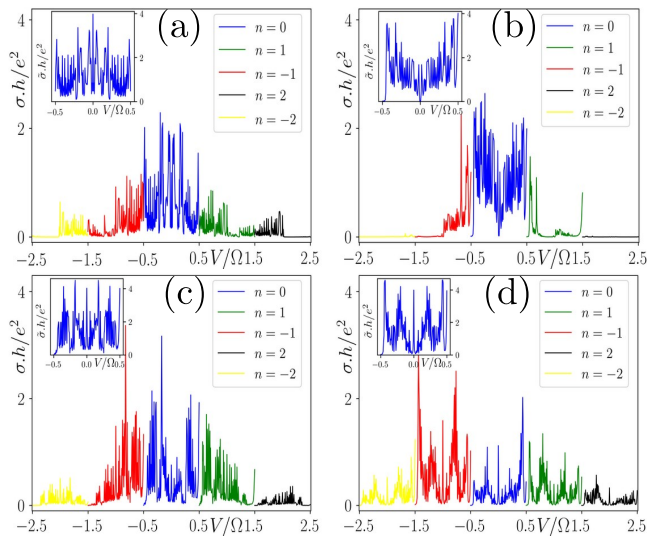


FIG. 4. In case of driven Rashba NW setup, the single-terminal differential conductance σ appearing from different photon sectors (their sum $\tilde{\sigma}$) are depicted in the panels (insets). Panel (a) [(b)] stands for the same considering single 0- $[\pi]$ FMEMs present at one end of the NW, representing case 1 [2]. On the other hand, the panels (c) and (d) both correspond to the simultaneous presence of a single 0-mode and a single π -mode at one end of the NW, capturing cases 3 and 4, respectively. For all the above cases, no single photon sector contributes alone to the quantized value. However, summed conductance $\tilde{\sigma}$ exhibits a quantized value of $4e^2/h$ at $V = 0$ and/or $V = \Omega/2$. Here, the model parameters are chosen as (a) $(c_0, c_1, \Omega, N) = (0.25, 0.25, 2.25, 110)$, (b) $(c_0, c_1, \Omega, N) = (1.0, -1.8, 4.5, 70)$, (c) $(c_0, c_1, \Omega, N) = (-0.45, -0.5, 2.24, 110)$ and (d) $(c_0, c_1, \Omega, N) = (0.8, 1.92, 1.49, 100)$. We choose $B_x = 1.0$ and all the other model parameters remain the same as mentioned in Fig. 2.

voltage $V + n\Omega$. However, the summed conductance $\tilde{\sigma}$ manifests a quantized peak of $4e^2/h$ at $V = 0$ [see the inset of Fig. 4(a)]. Then, Fig. 4(b) stands for the transport signature corresponding to case 2 with single π -mode. Here also $\tilde{\sigma}$ exhibits a quantized peak at $V = \Omega/2$ [see the inset of panel Fig. 4(b)] while contribution originating from the individual photon sectors σ exhibits no such quantization. Furthermore, Fig. 4(c) and (d) represent the transport signature for case 3 and case 4, respectively, with one 0- and one π -mode. In these above two cases, we also obtain the quantized nature of the summed conductance $\tilde{\sigma}$ at $V = 0$ and $V = \Omega/2$. Hence, our results are quite consistent with the well known Floquet sum rule [81] even in case of Rashba NW setup.

C. Stability against disorder

To investigate the robustness of $\tilde{\sigma}$ for the above mentioned cases, we introduce time-independent random on-

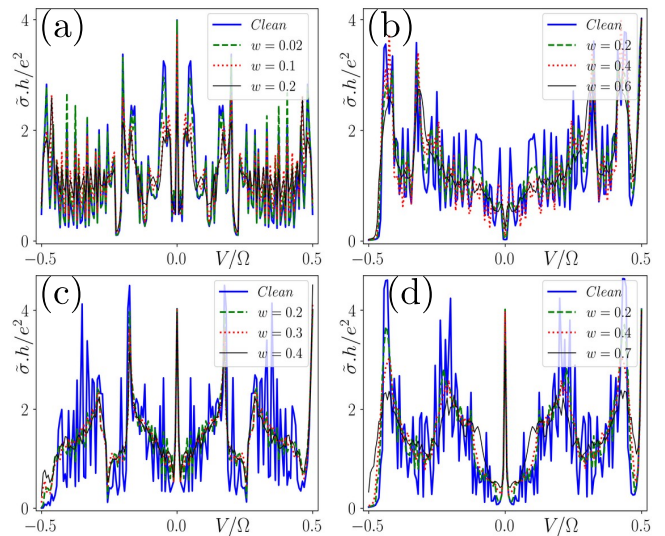


FIG. 5. We depict the disorder averaged one-terminal summed differential conductance $\tilde{\sigma}$ as a function of voltage bias V in the presence of random disorder. We here consider the same order for panels (a,b,c,d) corresponding to the cases 1, 2, 3, and 4, respectively as presented in Fig. 4. The value of chemical potential remains the same as mentioned in Fig. 4. We consider 100 disorder configurations for each case.

site chemical potential in the Hamiltonian [Eq. (1)] as

$$V_{\text{dis}} = V(r)\Gamma_1, \quad (11)$$

where $V(r)$ is randomly distributed over the range $[-\frac{w}{2}, \frac{w}{2}]$ with disorder strength given by w . Over the full time period of the drive, the lattice Hamiltonian with onsite disorder takes the form as

$$\begin{aligned} H_{\text{dis}}(t) &= H_1 + \sum_{j=1}^N \Psi_j^\dagger [V(r)\Gamma_1] \Psi_j; \quad t \in \left[0, \frac{T}{4}\right) \\ &= H_0 + \sum_{j=1}^N \Psi_j^\dagger [V(r)\Gamma_1] \Psi_j; \quad t \in \left[\frac{T}{4}, \frac{3T}{4}\right) \\ &= H_1 + \sum_{j=1}^N \Psi_j^\dagger [V(r)\Gamma_1] \Psi_j; \quad t \in \left[\frac{3T}{4}, T\right) \end{aligned} \quad (12)$$

Similar to the clean case as mentioned in the previous subsection, we compute $\tilde{\sigma}$ in the presence of disorder. We consider three disorder strengths for each case and perform an average over 100 disorder configurations. We illustrate our results in Fig. 5.

Here, Fig. 5(a) demonstrates the disorder study for case 1. The quantized value of $\tilde{\sigma}$ at $V = 0$ is quite stable against weak disorder ($w = 0.02$) and starts losing its quantization in moderate disorder limit ($w = 0.1, 0.2$). Similarly, Fig. 5(b) represents the same for case 2. Here also quantization of $\tilde{\sigma}$ at $V = \Omega/2$ remains unaffected

in weak ($w = 0.2$) and moderate ($w = 0.4$) disorder limit, and fails to retain the quantization (i.e., peak height decreases) towards strong ($w = 0.6$) disorder regime. Note that, weak (strong) disorder corresponds to its strength being smaller (larger) than the corresponding bulk gap and moderate disorder refers to the strength equivalent to the corresponding bulk gap. Furthermore, Fig. 5(c) (Fig. 5(d)) describes the case 3 (case 4). In both the instances, weak disorder cannot affect the quantization at $V = 0$ and $V = \Omega/2$. However, the scenario becomes different when we start increasing the disorder strength. At first, let us concentrate on Fig. 5(c). We find that $w = 0.3$ destroys the quantization at $V = \Omega/2$ while the peak height at $V = 0$ is unaffected. One has to increase the disorder strength to $w = 0.4$ to diminish its quantization. Therefore, in this case, the ZBP ($V = 0$) is more stable against disorder than the π bias ($V = \Omega/2$) peak. Nevertheless, Fig. 5(d) describes exactly the opposite picture to the previous case where π bias peak is found to be more stable than the zero bias one when disorder is present. Nonetheless, for both situations, a more stable peak is associated with a larger bulk gap (0 or π) which is expected in the study of disorder.

D. Transport signature for multiple FMEMs

After investigating the transport signature of single FMEM corresponding to a particular quasi-energy (0 or π) and located at one end of the NW, we here discuss the same for multiple FMEMs. To be precise, the driven system can host more than one FMEM for a particular quasi-energy at its one end. For completeness, we consider two cases: double 0- and double π -modes present at each end of the driven NW. For both the cases, we compute σ corresponding to each photon sector and depict them in Fig. 6(a) and Fig. 6(b) for 0- and π -modes respectively. Here also no individual photon sector gives rise to a quantized peak for σ . However, their sum exhibits a quantized peak with height $8e^2/h$ at $V = 0$ for the former case (double 0-modes) and for the latter (double π -modes) at $V = \Omega/2$ (see the insets of Fig. 6). The peak heights become doubled (instead of $4e^2/h$) due to the non edge resolved wavefunctions of multiple FMEMs.

V. ALTERNATIVE EXPERIMENTALLY FEASIBLE MODEL: HELICAL SHIBA CHAIN

After detailed investigations on transport signature of FMEMs in Rashba NW model, we concentrate on another realistic model known as helical Shiba chain which is based on magnetic impurity chain and superconductor heterostructure [20, 76]. In this setup, a chain of magnetic impurity atoms (with their magnetic moments forming a helical structure) is placed on the top of an s -wave superconducting substrate. The scattering between superconductor electrons and magnetic adatoms

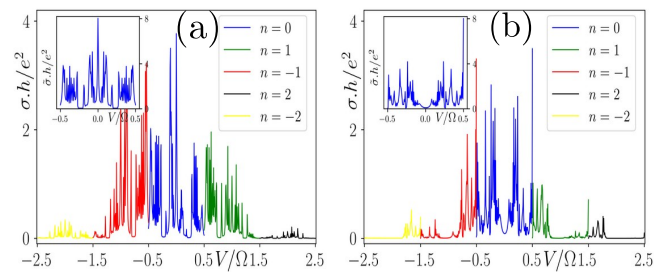


FIG. 6. (a) We depict the one terminal conductance σ as a function of bias voltage V choosing different photon sectors for double 0-modes in case of driven Rashba NW. The inset illustrates the quantized peak obtained via summed conductance $\bar{\sigma}$ for the same setup. (b) Here we repeat the same for π -modes. Note that, $\bar{\sigma}$ exhibits a quantized peak value of $8e^2/h$ at zero-(π -) bias voltage for the former (latter) case. We choose the model parameters as $(c_0, c_1, \Omega, N) = (0.5, -1, 2.25, 100)$ for panel (a) while $(1, 0.2, 2.4, 140)$ for panel (b). We choose $B_x = 1.0$ and all the other model parameters remain the same as mentioned in Fig. 2.

forms bound states termed as Shiba states. The hybridization among these Shiba states forms Shiba bands. These emerging bands host effective p -wave pairing that causes the MZMs to appear at the end of the chain [21]. Here, the band inversion takes place within the mini gap created between the two lowest Shiba bands leading to a topological phase transition. We begin by considering the following Bogoliubov-de Gennes (BdG) basis: $\Psi_j = \{c_{j\uparrow}, c_{j\downarrow}, c_{j\downarrow}^\dagger, -c_{j\uparrow}^\dagger\}^t$; where, $c_{j\uparrow}^\dagger$ ($c_{j\uparrow}$) and $c_{j\downarrow}^\dagger$ ($c_{j\downarrow}$) stand for quasi-particle creation (annihilation) operator for the spin-up and spin-down sector at a lattice site- j , respectively, and \mathbf{t} represents the transpose operation. Then following the above BdG basis, lattice Hamiltonian of a 1D Shiba chain with out-of-plane Néel-type spin spiral [33] is given by [20, 76]

$$H = \sum_{j=1}^N \Psi_j^\dagger [-\mu\Gamma_1 + B \cos(j\theta)\Gamma_2 + B \sin(j\theta)\Gamma_3 + \Delta\Gamma_4] \Psi_j + \sum_{j=1}^{N-1} \Psi_{j,\eta}^\dagger t_h \Gamma_1 \Psi_{j+1} + \text{H.c.}, \quad (13)$$

where, μ , B , θ , Δ , and t_h denote chemical potential, strength of the magnetic impurity, angle between two consecutive classical spins, superconductor gap of the parent s -wave superconductor and hopping amplitude, respectively. Here, $\Gamma_1 = \tau_z \sigma_0$, $\Gamma_2 = \tau_0 \sigma_z$, $\Gamma_3 = \tau_0 \sigma_x$, $\Gamma_4 = \tau_x \sigma_0$, with the Pauli matrices $\boldsymbol{\tau}$ and $\boldsymbol{\sigma}$ act on the particle-hole and spin (\uparrow, \downarrow) sub-spaces, respectively. Note that, the separation between two impurity atoms is large enough to neglect the spin-spin interaction between themselves. The Shiba chain hosts one pair of MZMs at its two ends in the topological superconducting regime which is given by $B_- < |B| < B_+$; with

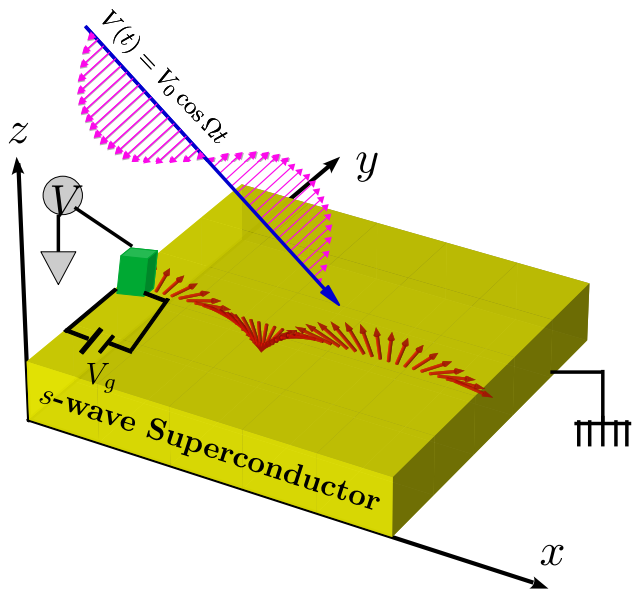


FIG. 7. Schematic diagram of our setup for helical Shiba chain model. A chain of magnetic adatoms (red arrows) is placed on the top of a common s -wave superconductor (lime green). The angle between the magnetic moments of two adjacent atoms is such that they form a helical structure (here out of plane Néel type). To change chemical potential a gate voltage V_g is applied. A metallic lead (green) is attached to one end of the chain. A bias voltage V is applied through the lead to study the differential conductance. The superconductor is connected to the ground. Applied periodic drive $V(t) = V_0 \cos \Omega t$ is also schematically depicted.

$B_{\pm} = \sqrt{\Delta^2 + (|\mu| \pm 2 \cos(\theta/2)t_h)^2}$ [20, 76]. It is interesting to note that $\theta = 0$ gives rise to the condition for topological phase transition in case of Rashba NW as mentioned in Sec. II. Such setup has been experimentally realized in Fe/Co/Mn/Cr adatoms deposited on the top of s -wave Nb/Pb/Re superconductor [42–50].

Let us consider the following external periodic drive protocol with chemical potential.

$$V(t) = \sum_{j=1}^N \Psi_j^\dagger [V_0 \cos(\Omega t) \Gamma_1] \Psi_j, \quad (14)$$

where, V_0 and $\Omega (= 2\pi/T)$ are the amplitude and frequency of the drive, respectively. The application of such drive gives rise to the topological phase transition within the emergent quasi-energy Shiba band hosting FMEMs at the ends of the chain. Here, 0 or π FMEMs appear even if one starts from the non-topological regime of the system [76].

First, we compute the static one terminal differential conductance σ_{stat} in the topological regime of this setup with large enough system size ($N=300$ sites). The ZBP with a quantized value of $2e^2/h$ manifests itself as a transport signature of static Majorana modes as shown in Fig. 8(a). The other non-quantized peaks (at non-zero V) in σ_{stat} correspond to the signature of Shiba bands.

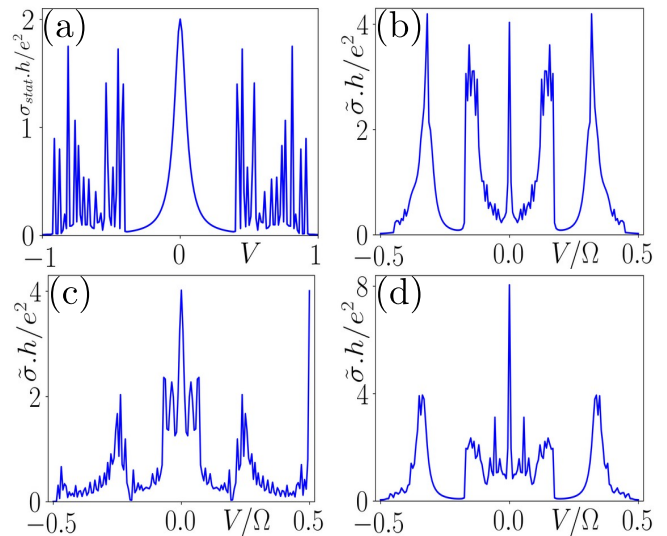


FIG. 8. (a) We depict the one terminal differential conductance σ_{stat} as a function of bias voltage for the static Shiba chain setup. We obtain a quantized peak with height $2e^2/h$ at $V = 0$. For the driven system we compute conductance $\tilde{\sigma}$ (summed over different photon sectors) considering the cases with single 0-mode, one 0- and one π -modes, and double 0-modes and illustrate them as a function of bias voltage in panels (b), (c), and (d), respectively. We obtain $4e^2/h$ quantization at $V = 0$ for panel (b) and at $V = 0$ and $V = \Omega/2$ for panel (c). In panel (d), ZBP manifests its quantized value of $8e^2/h$ due to double 0-FMEMs. We choose $B = 4$, $N=300$ lattice sites for panel (a). For panel (b) the parameters are chosen as $(B, N, V_0, \Omega) = (5, 100, 5, 7)$ and $(B, N, V_0, \Omega) = (2, 140, 5, 6)$ for panel (c). In panel (d), we choose $(B, N, V_0, \Omega) = (5, 120, 8, 4.2)$. The rest of the model parameters remain the same for all four panels: $(\mu, \Delta, t_h, \theta) = (4, 1, 1, 2\pi/3)$.

For periodically driven Shiba chain, we consider three cases for transport study: single 0-mode, one 0- and one π -mode, and double 0-modes that are located at the ends of the chain. Here also, not being able to consider large enough system sizes, we are bound to obtain the overlapped wave functions for FMEMs. We compute Floquet summed conductance $\tilde{\sigma}$ and depict them in Figs. 8(b), (c), and (d) corresponding the three cases respectively. We obtain a ZBP with a height of $4e^2/h$ as depicted in Fig. 8(b). The peak height remains the same for π -modes individually as shown in Fig. 8(c). On the other hand, Fig. 8(d) exhibits a ZBP with the quantized value of $8e^2/h$ when two 0-FMEMs are present. Hence, for all these cases mentioned for the Shiba chain, we obtain similar qualitative results for $\tilde{\sigma}$ as discussed in case of Rashba NW model.

VI. TRANSPORT RESULTS EMPLOYING NEGF TECHNIQUE

Having discussed about the transport signature of FMEMs employing an approximate analytical formula [Eq. (8)], we repeat our findings by applying purely numerical techniques with the help of NEGF. In order to carry that out, we attach another lead to the right end of the system. Then for applied bias V , the differential conductance for the driven system is given by (see Appendix C for details)

$$\begin{aligned}\tilde{\sigma}(V) &= -2\pi e^2 \int d\omega \sum_n \mathbf{T}_{LL}^{(n)} [f'^L(\omega) + f'^R(-\omega)] \\ &+ 2\pi e^2 \int d\omega \sum_n [\mathbf{T}_{LR}^{(n)} f'^R(\omega) - \mathbf{T}_{RL}^{(n)} f'^L(\omega)] \\ &= \sum_n \sigma(V + n\Omega),\end{aligned}\quad (15)$$

where, $\mathbf{T}_{\lambda\lambda'}^{(n)}(\omega) = \text{Tr} [\mathbf{G}^{(n)\dagger}(\omega) \mathbf{V}^{\lambda t} \mathbf{G}^{(n)}(\omega) \mathbf{V}^{\lambda'}]$ and $\lambda, \lambda' \in L, R$ denote the lead indices. For the static case, the zero frequency limit of the above equation gives rise to the corresponding expression for differential conductance σ_{stat} as

$$\begin{aligned}\sigma_{\text{stat}}(V) &= -2\pi e^2 \int d\omega \mathbf{T}_{LL} [f'^L(\omega) + f'^R(-\omega)] \\ &+ 2\pi e^2 \int d\omega [\mathbf{T}_{LR} f'^R(\omega) - \mathbf{T}_{RL} f'^L(\omega)].\end{aligned}\quad (16)$$

Here, $\mathbf{T}_{\lambda\lambda'}(\omega) = \text{Tr} [\mathbf{G}^\dagger(\omega) \mathbf{V}^{\lambda t} \mathbf{G}(\omega) \mathbf{V}^{\lambda'}]$ with $\mathbf{G}(\omega) = [\omega \mathbf{I} - \mathbf{H} + i\epsilon \mathbf{I}]^{-1}$ with infinitesimally small positive value of ϵ .

A. Rashba NW

We illustrate our transport results in Fig. 9 for the Rashba NW using NEGF technique. For static NW, we compute differential conductance σ_{stat} using Eq. (16) and illustrate as a function of bias voltage V in Fig. 9(a). Like previous method, we obtain the ZBP to be quantized with the value $2e^2/h$. For the driven Rashba NW case, we compute differential conductance considering individual photon sectors σ and their sum $\tilde{\sigma}$ using Eq. (15). The corresponding results are depicted in Fig. 9(b) and (c) considering one 0-, one π -FMEMs and double π -FMEMs, respectively. Here also akin to the earlier method, no photon sector solely gives rise to the quantized peak for σ while their sum $\tilde{\sigma}$ exhibits quantization of $2e^2/h$ at $V = 0$ and $V = \Omega/2$ for the former case [see the inset of Fig. 9(b)] and $4e^2/h$ at $V = \pm\Omega/2$ for the latter case as shown in the inset of Fig. 9(c). We also present disorder stability of $\tilde{\sigma}$ considering one 0-, one π -FMEMs in Fig. 9(d). Note that, quantized peak height remains

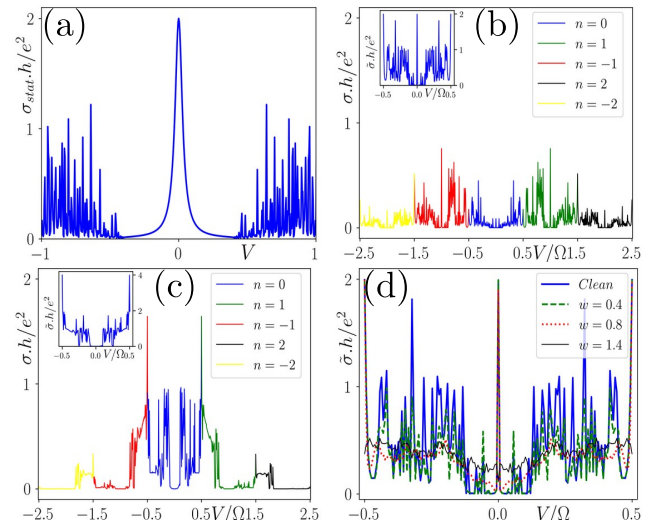


FIG. 9. We depict two terminal differential conductance as a function of bias voltage V using NEGF technique for the static and driven Rashba NW case. (a) We repeat the inset of Fig. 2 using Eq. (16) for static case considering $N = 120$ lattice sites. We obtain $2e^2/h$ quantization of ZBP for σ_{stat} . Panels (b) and (c) represent the NEGF technique counterpart of Fig. 4(d) and Fig. 6(b) having one 0 - one π -FMEMs and two π -FMEMs, respectively. We obtain corresponding summed conductance $\tilde{\sigma}$ to be quantized at $V = 0$ and $V = \Omega/2$ with peak height $2e^2/h$ for single FMEM and $4e^2/h$ for double FMEMs, respectively. (d) We illustrate disorder stability of FMEMs corresponding to panel (b). We observe that for weak disorder limit, quantization of $\tilde{\sigma}$ remains unaffected. However, strong disorder destroys the quantization of peak height. We consider all the model parameters to be the same as mentioned before.

robust against weak disorder strength while loses quantization completely for strong disorder strength. Therefore, our NEGF results match well with the results obtained from approximate analytical formula [Eq. (8)].

B. Helical Shiba Chain

We depict our NEGF results for the helical Shiba chain in Fig. 10. Here, Fig. 10(a) represents σ_{stat} for the static Shiba chain while Fig. 10(b) stands for $\tilde{\sigma}$ considering double 0-FMEMs emerged in driven Shiba chain setup. We obtain ZBP of σ_{stat} ($\tilde{\sigma}$) to be quantized with the peak height $2e^2/h$ ($4e^2/h$) for the static MZM (double 0-FMEMs). Hence, in case of Shiba chain also we obtain the same results using NEGF as the earlier case.

Note that for both the models, unlike the previous method, the extra 2 factor in quantized peak is absent as a consequence of the fact that NEGF method does not require the underlying end-resolved property of the wave functions associated with MEMs.

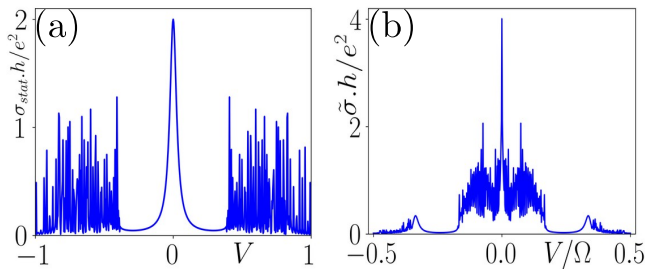


FIG. 10. Here, we depict two terminal differential conductance as a function of bias voltage V using NEGF technique for the static and driven Shiba chain model. In panels (a) and (b), we repeat Fig. 8(a) [static case] considering $N = 100$ lattice sites and Fig. 8(d) [driven system with double 0-FMEMs] respectively using Eq. (16). We obtain $2e^2/h$ [$4e^2/h$] quantization of ZBP for σ_{stat} [$\tilde{\sigma}$] in panel (a) [(b)]. All the model parameters remain same as mentioned in Fig. 8.

VII. EXPERIMENTAL FEASIBILITY

In this section, we discuss possible experimental connection to realize our numerical findings regarding transport signature of FMEMs.

A. Rashba NW

In case of Rashba NW, as far as experimental feasibility is concerned, suitable candidate can be InAs/InSb NW having strong SOC and placed on the top of Nb/Al (s -wave superconductor). Au can do the job for metallic lead [15]. Three step drive protocol [Eq. (12)] may be applied via time dependent gate voltage [86–89], by choosing proper superposition of several harmonics. Note that, for $0 \leq t < T/4$ and $3T/4 \leq t < T$ the system acts as an atomic insulator without any hopping. Hence, in these time domains gate voltage and other control parameters need to be tuned in such a way that the bands remain relatively flat and largely gapped. The band dispersion comes into the picture only in the middle half of the drive ($T/4 \leq t < 3T/4$). To obtain possible experimental signature of one 0- and one π - FMEMs e.g., Fig. 4(d), following parameters may be considered: reported value for Rashba SOC ($2u$) in InSb is around $50 \mu\text{eV}$ [14]. Our numerical computation suggests $t_h = 2u = \Delta = B_x = 50 \mu\text{eV}$, $c_1 = 0.8t_h = 40 \mu\text{eV}$, $c_1 = 1.92t_h = 96 \mu\text{eV}$, and $\Omega = 1.49t_h \approx 18 \text{ GHz}$.

B. Helical Shiba chain

For Shiba chain model, Nb (110) can be one good choice with large superconducting gap $\Delta = 1.51 \text{ meV}$ [90]. Afterwards, Mn/Cr magnetic adatoms can be fabricated on top of Nb (110) substrate by using

STM-based single-atom manipulation technique [44, 45, 49, 91]. This method provides a better tunability for the angles between spin of the impurity atoms [42]. For this case also, Au can be the suitable choice for metallic lead. External sinusoidal drive can be applied via AC gate voltage. To obtain possible transport signature e.g., Fig. 8(b), our numerical computation suggest the model parameters to have values: $t_h = \Delta = 1.51 \text{ meV}$, $B = 2\Delta = 3.02 \text{ meV}$, $V_0 = 5\Delta = 7.55 \text{ meV}$, and $\Omega \approx 1.45 \text{ THz}$.

VIII. SUMMARY AND CONCLUSIONS

To summarise, in this article, we explore the transport signature of single and multiple FMEMs in two experimentally feasible setups: first one is Rashba NW and the second one is helical Shiba chain model based on magnet-superconductor heterostructure. Initially, we begin with a 1D NW, having strong Rashba SOC and Zeeman field oriented along its length, that is placed in close proximity to an s -wave superconductor. The system can effectively mimic the 1D p -wave Kitaev chain by hosting MZMs at the two ends of the NW. We study the transport signature of these MZMs by computing one-terminal static differential conductance σ_{stat} . We obtain a ZBP with quantized peak height $2e^2/h$ for σ_{stat} as the indirect signature of MZMs [81]. Thereafter, we adopt a three-step periodic drive protocol in this model to engineer anomalous π -modes in addition to regular 0-modes. One can have a control over the number of FMEMs by regulating the frequency and amplitude of the drive [75]. We obtain $2 \times 2e^2/h$ quantization for both types of FMEMs as their wave functions are not end-resolved due to the finiteness of the system.

We also explore the stability of these quantized peaks against static random onsite disorder. We observe that the quantization remains robust in the limit of small disorder strength and the peak height loses its quantization in the limit of moderate or high disorder limit depending on the 0 or π gap. We find that the peaks due to FMEMs associated with larger bulk gaps exhibit better stability against disorder. For multiple FMEMs, we obtain the corresponding quantized value $n \times 2 \times 2e^2/h$ with n being number of FMEMs that are localized at one end for a large enough system. We repeat our study for helical Shiba chain model [20, 21, 76] and obtain similar results as compared to Rashba NW. We validate our investigation using the microscopic NEGF framework. We obtain a quantized peak of $n \times 2e^2/h$ for differential conductance corresponding to n number of FMEMs present at one end of the system. Interestingly, the extra 2 factor does not arise for NEGF while it appears in the previous method as the wave-functions under interest have a common spatial overlap at one end of the system. Finally we discuss the experimental feasibility of our findings for both the models.

Under application of external periodic drive, the con-

cerned two realistic systems host multiple FMEMs. Braiding among these non-equilibrium Majorana modes can establish themselves as suitable candidates for fault-tolerant quantum computations. However, primarily experimental detection of them is necessary before proposing any such kind of application. Transport signature is a very important tool as far as the detection of topological FMEMs is concerned. Hence, our study paves the way towards the detection of multiples FMEMs in realistic model systems. The investigation of Shot noise and Josephson current signature of FMEMs in these realistic models can be interesting future directions as well.

Acknowledgments

We acknowledge Arijit Kundu, Arnob Kumar Ghosh, Amartya Pal, and Kamalesh Bera for stimulating discussions. DM thanks Dipak Maity and Sanu Varghese for technical help.

Appendix A: Notations

Throughout all the appendices, we use the following notations for indices. Greek letters like $\bar{\alpha}$, $\bar{\beta}$ are used to denote the eigenvalue indices and α , β stand for site indices in the leads. We consider i , j , l for site indices in the system while k , m , n indicate frequency indices. Furthermore, λ , λ' represent lead indices (left L or right R). Superscript index c is used for contact site of the system. The s and s' indices represent spin/chiral degrees of freedom. Note that, bold notation in equations corresponds to matrix representation and corresponding superscript T stands for transpose operation. Also, repeated indices follow Einstein's summation rule. We consider $\hbar = 1$ following the natural unit.

Appendix B: A primer to Floquet theory

For a periodically driven system i.e., $H(t+T) = H(t)$, Schrödinger's equation can be written as [81, 84, 85]

$$i \frac{d}{dt} |\psi(t)\rangle = (H(t) - i\Sigma) |\psi(t)\rangle, \quad (\text{B1})$$

where Σ denotes the environmental degrees of freedom emerging due to the bath attached to the system. This makes the time evolution non-unitary where T is the time period of the drive. Following the analogy of the Bloch theorem, we consider the ansatz as

$$|\psi_{\bar{\alpha}}(t)\rangle = e^{-i(\epsilon_{\bar{\alpha}} - i\delta_{\bar{\alpha}})t} |u_{\bar{\alpha}}(t)\rangle, \quad (\text{B2})$$

with $|u_{\bar{\alpha}}(t)\rangle = |u_{\bar{\alpha}}(t+T)\rangle$. Here, $|u_{\bar{\alpha}}(t)\rangle$ are called Floquet states and $\epsilon_{\bar{\alpha}}$ are called quasi-energies with width $\delta_{\bar{\alpha}}$. Inserting the following ansatz in Eq. (B1) we have

$$\left(H(t) - i\Sigma - i \frac{d}{dt} \right) |u_{\bar{\alpha}}(t)\rangle = (\epsilon_{\bar{\alpha}} - i\delta_{\bar{\alpha}}) |u_{\bar{\alpha}}(t)\rangle. \quad (\text{B3})$$

The above equation is called Floquet-Schrödinger's equation. Time evolution operator is given by

$$U(t, t') = \text{TO} \left[e^{-i \int_{t'}^t H(s) ds} \right]. \quad (\text{B4})$$

Note that, for a periodically driven system, time evolution operator is also periodic i.e., $U(t+T, T) = U(t, 0)$. Then, $U(t+T, t) |\psi(t)\rangle = |\psi(t+T)\rangle$. Using Eq. (B2) and periodicity of $|u_{\bar{\alpha}}(t)\rangle$, we have

$$U(t+T, t) |u_{\bar{\alpha}}(t)\rangle = e^{-i(\epsilon_{\bar{\alpha}} - i\delta_{\bar{\alpha}})T} |u_{\bar{\alpha}}(t)\rangle. \quad (\text{B5})$$

For a non-interacting system, if $\Lambda_{\bar{\alpha}}$ are the energy eigenvalues of $U(T, 0)$, then the quasi-energies are given by $\epsilon_{\bar{\alpha}} = \frac{i}{T} \ln(\Lambda_{\bar{\alpha}})$. Note that, in Eq. (B5) if we substitute $\epsilon_{\bar{\alpha}} \rightarrow \epsilon_{\bar{\alpha}} + n\Omega$ with $n \in \mathbb{Z}$, and $\Omega = 2\pi/T$, then we obtain new $|u_{\bar{\alpha}}(t)\rangle \rightarrow e^{in\Omega t} |u_{\bar{\alpha}}(t)\rangle$ for the same set of $\{|\psi_{\bar{\alpha}}(t)\rangle\}$. Thus quasi-energies for Floquet states are not unique and are connected via external periodic drive by emission and absorption of virtual photons. Due to this reason we call these frequency indices as photon sectors as long as Floquet theory is concerned. Although quasi-energies are unique within 1st Floquet zone or 0th photon sector: $-\Omega/2 \leq \epsilon_{\bar{\alpha}} \leq \Omega/2$. Since the Floquet states are time periodic, we can write them in terms of Fourier modes as

$$|u_{\bar{\alpha}}(t)\rangle = \sum_n e^{-in\Omega t} |u_{\bar{\alpha}}^{(n)}\rangle, \\ \text{with } |u_{\bar{\alpha}}^{(n)}\rangle = \int_0^T \frac{dt}{T} e^{in\Omega t} |u_{\bar{\alpha}}(t)\rangle. \quad (\text{B6})$$

One can perform the same for time periodic total Hamiltonian, $H_{\text{tot}} = H(t) - i\Sigma$. Then in frequency space Floquet Schrodinger's equation looks like

$$H_{\text{tot}}^{(k-n)} |u_{\bar{\alpha}}^{(n)}\rangle = (\epsilon_{\bar{\alpha}} - i\delta_{\bar{\alpha}} + k\Omega) |u_{\bar{\alpha}}^{(k)}\rangle, \quad (\text{B7})$$

with $H_{\text{tot}}^{(k-n)} = \int_0^T \frac{dt}{T} e^{i(k-n)\Omega t} H_{\text{tot}}(t)$. Here, the time evolution is non-unitary due to the presence of Σ . Hence, we have to deal with bi-orthogonalization of non-Hermitian system. The left eigen vectors $|u_{\bar{\alpha}}^{\pm}(t)\rangle$ is given by

$$\left(H(t) + i\Sigma - i \frac{d}{dt} \right) |u_{\bar{\alpha}}^{\pm}(t)\rangle = (\epsilon_{\bar{\alpha}} \pm i\delta_{\bar{\alpha}}) |u_{\bar{\alpha}}^{\pm}(t)\rangle. \quad (\text{B8})$$

The eigenstates of $U(T, 0)$ yields the bi-orthogonalisation and completeness relations as

$$\frac{1}{T} \int_0^T dt \langle u_{\bar{\alpha}}^{\pm}(t) | u_{\bar{\beta}}^{\pm}(t) \rangle = \delta_{\bar{\alpha}\bar{\beta}}, \\ \text{and } \sum_{\bar{\alpha}} |u_{\bar{\alpha}}(t)\rangle \langle u_{\bar{\alpha}}^{\pm}(t)| = \mathbf{I}. \quad (\text{B9})$$

In frequency space these two relations have the form as

$$\sum_k \langle u_{\bar{\alpha}}^{+(k)} | u_{\bar{\beta}}^{(k)} \rangle = \delta_{\bar{\alpha}\bar{\beta}}, \\ \text{and } \sum_{\bar{\alpha}, k} |u_{\bar{\alpha}}^{(k)}\rangle \langle u_{\bar{\alpha}}^{+(k)}| = \mathbf{I}. \quad (\text{B10})$$

In this scenario, the time evolution operator is given by

$$U(t, t') = \sum_{\bar{\alpha}} e^{-i(\epsilon_{\bar{\alpha}} - i\delta_{\bar{\alpha}})(t-t')} |u_{\bar{\alpha}}(t)\rangle \langle u_{\bar{\alpha}}^{\dagger}(t')|. \quad (\text{B11})$$

Note that, $U(t, t')$ is the two points correlation function in time domain i.e. retarded Green's function $G(t, t')$ in the context of dynamics of a system. We use this in the next section to calculate the conductance for a driven system.

Appendix C: Transport theory for Floquet Majorana modes

Let us consider a periodically driven system attached to the leads as mentioned before. The Hamiltonian corresponding to the system, leads and coupling between them can be written as [69, 81–83, 92]

$$H_s(t) = \sum_{i,j} H_{ij}(t) c_i^{\dagger} c_j \equiv \mathbf{c}^{\dagger} \mathbf{H}(t) \mathbf{c}, \quad (\text{C1})$$

$$\begin{aligned} H_{L/R} &= \sum_{\lambda} H_{L/R}^{\lambda} = \sum_{\lambda, \alpha, \beta} F_{\alpha\beta}^{\lambda} a_{\alpha}^{\lambda\dagger} a_{\beta}^{\lambda} \\ &\equiv \mathbf{a}^{\dagger\lambda} \mathbf{F}^{\lambda} \mathbf{a}^{\lambda}, \end{aligned} \quad (\text{C2})$$

$$\begin{aligned} H_c &= \sum_{\lambda} H_c^{\lambda} = \sum_{\lambda, \alpha, i} K_{\alpha, i}^{\lambda} a_{\alpha}^{\lambda\dagger} c_i + h.c. \\ &\equiv \sum_{\lambda} \mathbf{a}^{\dagger} \mathbf{K}^{\lambda} \mathbf{c} + h.c. \end{aligned} \quad (\text{C3})$$

Here, a/c (a^{\dagger}/c^{\dagger}) denote the electronic annihilation (creation) operators for the lead/system, respectively. Also, λ stands for the λ^{th} lead at left/right sides of the system. The sum of the above three Hamiltonians can be written as $H_{\text{Total}}(t) = H_s(t) + H_c + H_{L/R}$.

Heisenberg equation of motion (EOM) for lead operator a_{α}^{λ} is given by

$$\begin{aligned} \dot{a}_{\alpha}^{\lambda} &= -i [a_{\alpha}^{\lambda}, H_{\text{Total}}(t)] \\ &= -i [a_{\alpha}^{\lambda}, H_s(t) + H_c + H_{L/R}] \\ &= -i F_{\alpha\beta}^{\lambda} a_{\beta}^{\lambda} - i K_{\alpha l}^{\lambda} c_l. \end{aligned} \quad (\text{C4})$$

Similarly, EOM for the system electronic operator c_j is given by

$$\dot{c}_j = -i H_{jl}(t) c_l - i K_{\alpha j}^{\lambda*} a_{\alpha}^{\lambda}. \quad (\text{C5})$$

Rewriting Eq. (C4), we obtain

$$\left(i\delta_{\alpha\beta} \frac{d}{dt} - F_{\alpha\beta}^{\lambda} \right) a_{\beta}^{\lambda} = K_{\alpha l}^{\lambda} c_l. \quad (\text{C6})$$

The Green's function $g_{\beta\nu}^{\lambda}(t, t') = \langle a_{\beta}(t) a_{\nu}^{\dagger}(t') \rangle$ for the leads can be derived from the above equation and is given by

$$\begin{aligned} g_{\beta\nu}^{\lambda}(t, t') &= -ie^{-iF_{\beta\nu}^{\lambda}(t-t')} \theta(t-t') \\ &\equiv [g^{\lambda}(t-t')]_{\beta\nu}. \end{aligned} \quad (\text{C7})$$

The solution of Eq. (C6) is given by $a_{\alpha}^{\lambda}(t) =$ complementary function (CF) + particular integral (PI) i.e.,

$$\begin{aligned} a_{\alpha}^{\lambda}(t) &= i [g^{\lambda}(t-t_0)]_{\alpha\beta} a_{\beta}^{\lambda}(t_0) \\ &\quad + \int_{t_0}^t dt' [g^{\lambda}(t-t')]_{\alpha\beta} K_{\beta l}^{\lambda} c_l(t'), \end{aligned} \quad (\text{C8})$$

where t_0 is the initial time which can be considered as distant past i.e., $-\infty$.

With the help of Eq. (C8), we can rewrite Eq. (C5) as

$$\begin{aligned} &\left[i\delta_{jl} \frac{d}{dt} - H_{jl}(t) \right] c_l(t) \\ &- i \int_{-\infty}^t dt' \Gamma_{jl}(t-t') c_l(t') = h_j(t), \end{aligned} \quad (\text{C9})$$

where, the coupling Γ_{jl} , and the noise h_j in the lead are defined as

$$\Gamma_{jl}(t-t') = -i K_{\alpha j}^{\lambda*} [g(t-t')]_{\alpha\beta} K_{\beta l}^{\lambda}, \quad (\text{C10})$$

$$\begin{aligned} h_j(t) &= \sum_{\lambda} h_j^{\lambda}(t) \\ &= i K_{\alpha j}^{\lambda*} [g(t-t_0)]_{\alpha\beta} a_{\beta}^{\lambda}(t_0). \end{aligned} \quad (\text{C11})$$

The thermal correlation is defined as

$$\langle h_j^{\lambda\dagger}(t) h_l^{\lambda'}(t') \rangle = K_{\alpha j}^{\lambda} g_{\alpha\beta}^{\lambda*}(t) K_{\gamma l}^{\lambda'*} g_{\gamma\delta}^{\lambda'}(t') \langle a_{\beta}^{\lambda\dagger}(t) a_{\delta}^{\lambda'}(t') \rangle \quad (\text{C12})$$

We can write lead Green's function in terms of lead energy eigenbasis as

$$g_{\mu\nu}^{\lambda}(t) = -i\theta(t) \sum_{\epsilon^{\lambda}} \langle \mu | \epsilon^{\lambda} \rangle \langle \epsilon^{\lambda} | \nu \rangle e^{-i\epsilon^{\lambda} t}. \quad (\text{C13})$$

Let us define density of states matrix in frequency space as

$$\rho_{\gamma\alpha}^{\lambda}(\omega) = \sum_{\epsilon^{\lambda}} \langle \gamma | \epsilon^{\lambda} \rangle \langle \epsilon^{\lambda} | \alpha \rangle \delta(\omega - \epsilon^{\lambda}). \quad (\text{C14})$$

Then thermal correlation in frequency space is given by

$$\begin{aligned} \langle h_j^{\lambda\dagger}(\omega) h_l^{\lambda'}(\omega') \rangle &= (2\pi)^2 \rho_{\gamma\alpha}^{\lambda}(\omega) K_{\alpha j}^{\lambda} K_{\gamma l}^{\lambda'*} \delta_{\lambda\lambda'} \delta(\omega - \omega') \\ &\quad \times f(\omega, \mu_{\lambda}, T_{\lambda}) \\ &\equiv (2\pi)^2 \mathbf{V}_{jl}^T \delta_{\lambda\lambda'} \delta(\omega - \omega') f(\omega, \mu_{\lambda}, T_{\lambda}), \end{aligned} \quad (\text{C15})$$

where, $\mathbf{V}^{\lambda} = \mathbf{K}^{\lambda\dagger} \rho^{\lambda} \mathbf{K}^{\lambda}$ and $f(\omega, \mu_{\lambda}, T_{\lambda})$ is the Fermi distribution function of the reservoir. Here, μ_{λ} , T_{λ} denote the chemical potential and temperature of the reservoirs, respectively.

Afterwards, changing the variable $\tau = t - t'$ in Eq. (C9), one can obtain

$$\left[i\delta_{jl} \frac{d}{dt} - H_{jl}(t) \right] c_l(t) - i \int_0^{\infty} d\tau \Gamma_{jl}(\tau) c_l(t-\tau) = h_j(t). \quad (\text{C16})$$

Introducing the Green's function $G_{ij}(t, t') = \langle c_i(t) c_j^\dagger(t') \rangle$, in matrix notation we have

$$\left[i\mathbf{I} \frac{d}{dt} - \mathbf{H}(t) \right] \mathbf{G}(t, t') - i \int_0^\infty d\tau \mathbf{\Gamma}(\tau) \mathbf{G}(t - \tau, t') = \delta(t - t') \mathbf{I}. \quad (\text{C17})$$

For any arbitrary t , and t' the above equation satisfies $\mathbf{G}(t, t') = \mathbf{G}(t+T, t'+T)$. Hence, we can perform Fourier transform (FT) for both the t , and t' . At first, let's perform the FT with respect to t' and we have

$$\mathbf{G}(t, \omega) = \int_{-\infty}^t dt' \mathbf{G}(t, t') e^{i\omega(t-t')} \quad (\text{C18})$$

$$= \int_0^\infty d\tau \mathbf{G}(t, t - \tau) e^{i\omega\tau}. \quad (\text{C19})$$

Now, taking FT with respect to t , we obtain

$$\mathbf{G}^{(k)}(\omega) = \frac{1}{T} \int_0^T dt e^{ik\Omega t} \mathbf{G}(t, \omega), \quad (\text{C20})$$

Using these two equations, Eq. (C17) becomes

$$\begin{aligned} & \left[i\mathbf{I} \frac{d}{dt} - \mathbf{A}(t) \right] \int_{-\infty}^\infty \frac{d\omega}{2\pi} \mathbf{G}(t, \omega) e^{-i\omega(t-t')} - i \int_0^\infty d\tau \mathbf{\Gamma}(\tau) \int_{-\infty}^\infty \frac{d\omega}{2\pi} \mathbf{G}(t - \tau, \omega) e^{-i\omega(t-\tau-t')} = \delta(t - t') \mathbf{I} \\ \implies & \int_{-\infty}^\infty \frac{d\omega}{2\pi} e^{-i\omega(t-t')} \left[i\mathbf{I} \frac{d}{dt} + \omega - \mathbf{A}(t) \right] \mathbf{G}(t, \omega) - i \int_0^\infty d\tau \mathbf{\Gamma}(\tau) \int_{-\infty}^\infty \frac{d\omega}{2\pi} \mathbf{G}(t - \tau, \omega) e^{-i\omega(t-\tau-t')} = \int_0^\infty \frac{d\omega}{2\pi} e^{-i\omega(t-t')} \mathbf{I}. \end{aligned}$$

Comparing both sides, we obtain

$$\left[i\mathbf{I} \frac{d}{dt} + \omega - \mathbf{A}(t) \right] \mathbf{G}(t, \omega) - i \int_0^\infty d\tau \mathbf{\Gamma}(\tau) \mathbf{G}(t - \tau, \omega) e^{i\omega\tau} = \mathbf{I}. \quad (\text{C24})$$

Note: Here, we assume that $t > 0$, and $\lim_{t' \rightarrow t-} G(t, t') = 0$.

Therefore, the solution for system electronic operators is given by

$$\begin{aligned} c_l(t) &= \int_{-\infty}^t dt' [G(t, t')]_{lj} h_j(t') \\ &= \int \frac{d\omega}{2\pi} G_{lj}(t, \omega) h_j(\omega) e^{-i\omega t} \quad (\text{C25}) \\ &= \int \frac{d\omega}{2\pi} e^{-i\omega t} e^{-ik\Omega t} G_{lj}^{(k)}(\omega) h_j(\omega), \quad (\text{C26}) \end{aligned}$$

where, $\mathbf{G}^{(k)}(\omega)$ is called the Nambu-Gorkov Green's function and is given by [69]

$$\mathbf{G}^{(k)}(\omega) = \sum_{\bar{\alpha}, n} \frac{|u_{\bar{\alpha}}^{(k+n)}\rangle \langle u_{\bar{\alpha}}^{+(n)}|}{\omega - \epsilon_{\bar{\alpha}} - n\Omega + i\delta_{\bar{\alpha}}}. \quad (\text{C27})$$

Number operator for electron in λ^{th} lead is, $N^\lambda(t) = a_\alpha^{\lambda\dagger}(t) a_\alpha^\lambda(t)$. Hence, Heisenberg EOM yields $\dot{N}^\lambda(t) = -i[N^\lambda(t), H_{\text{Total}}]$. The net current flowing across the

which yields inverse FT as

$$\mathbf{G}(t, \omega) = \sum_k e^{-ik\Omega t} \mathbf{G}^{(k)}(\omega). \quad (\text{C21})$$

Inverting Eqs. (C18) and (C19) we have

$$\mathbf{G}(t, t - \tau) = \frac{1}{2\pi} \int_{-\infty}^\infty d\omega \mathbf{G}(t, \omega) e^{-i\omega\tau}, \quad (\text{C22})$$

$$\mathbf{G}(t, t') = \frac{1}{2\pi} \int_{-\infty}^\infty d\omega \mathbf{G}(t, \omega) e^{-i\omega(t-t')}. \quad (\text{C23})$$

λ^{th} contact into the system can be given by

$$\begin{aligned} J^\lambda(t) &= (-e) \times (-\dot{N}^\lambda(t)) \\ &= -ie [N^\lambda(t), H_{\text{Total}}] \\ &= -ie \left(K_{\alpha l}^\lambda a_\alpha^{\lambda\dagger}(t) c_l(t) - K_{\alpha l}^{\lambda*} c_l^\dagger(t) a_\alpha^\lambda(t) \right) \quad (\text{C28}) \end{aligned}$$

Taking average over the lead states, one can obtain

$$\langle J^\lambda(t) \rangle = 2e \text{Im} [K_{\alpha l}^\lambda \langle a_\alpha^{\lambda\dagger}(t) c_l(t) \rangle].$$

Using the solution of $a_\alpha^\lambda(t)$ from Eq. (C8) and with the help of Eq. (C11) we can write

$$\begin{aligned} \langle J^\lambda(t) \rangle &= 2e \text{Im} \left[\langle h_l^{\lambda\dagger}(t) c_l(t) \rangle \right] \\ &\quad + 2e \text{Im} \left[\int_{-\infty}^t dt' K_{\alpha l}^\lambda g_{\alpha\beta}^{\lambda*}(t - t') K_{\beta j}^{\lambda*} \langle c_j^\dagger(t') c_l(t) \rangle \right] \\ &= \langle J_1^\lambda(t) \rangle + \langle J_2^\lambda(t) \rangle. \quad (\text{C29}) \end{aligned}$$

Analysis of the first term $\langle J_1^\lambda(t) \rangle$: Using the solution of $c_l(t)$ from Eq. (C25), and transforming to the frequency

space with the help of Eq. (C15) we obtain

$$\langle J_1^\lambda(t) \rangle = 2e \int d\omega f^\lambda(\omega) \text{Tr} \left[\left(\frac{\mathbf{G}(t, \omega) - \mathbf{G}^\dagger(t, \omega)}{2i} \right) \mathbf{V}^\lambda(\omega) \right].$$

Then taking Hermitian conjugate of Eq. (C24), and changing the variable ω to ω' one can obtain,

$$\mathbf{G}^\dagger(t, \omega') \left[-i\mathbf{I} \frac{d}{dt} + \omega' - \mathbf{A}(t) \right] + i \int_0^\infty d\tau e^{-i\omega'\tau} \mathbf{G}^\dagger(t - \tau, \omega') \mathbf{\Gamma}^\dagger(\tau) = \mathbf{I}. \quad (\text{C30})$$

Operating $-\mathbf{G}^\dagger(t, \omega') \times$ Eq. (C24) + Eq. (C30) $\times \mathbf{G}(t, \omega)$ yields the following equation mentioned below

$$\frac{\mathbf{G}(t, \omega) - \mathbf{G}^\dagger(t, \omega)}{2i} = -\frac{1}{2}\mathbf{I} \frac{d}{dt} [\mathbf{G}^\dagger(t, \omega) \mathbf{G}(t, \omega)] + \int_0^\infty d\tau \text{Re} [\mathbf{G}^\dagger(t, \omega) e^{i\omega\tau} \mathbf{\Gamma}(\tau) \mathbf{G}(t - \tau, \omega)]. \quad (\text{C31})$$

Let us decompose $\langle J_1^\lambda(t) \rangle$ into two parts:

$$\begin{aligned} \langle J_1^\lambda(t) \rangle &= \langle J_{11}^\lambda(t) \rangle + \langle J_{12}^\lambda(t) \rangle \\ &= \text{I} + \text{II}, \end{aligned} \quad (\text{C32})$$

Using Eq. (C31), we can write the first part (I) as

$$\begin{aligned} \langle J_{11}^\lambda(t) \rangle &= -e \frac{d}{dt} \int d\omega f^\lambda(\omega) \text{Tr} [\mathbf{G}^\dagger(t, \omega) \mathbf{G}(t, \omega) \mathbf{V}^\lambda(\omega)] \\ \implies \langle\langle J_{11}^\lambda \rangle\rangle &= \frac{1}{T} \int_0^T dt \langle J_{11}^\lambda(t) \rangle \\ \implies \langle\langle J_{11}^\lambda \rangle\rangle &= -e \int d\omega f^\lambda(\omega) \text{Tr} [\mathbf{G}^\dagger(t, \omega) \mathbf{G}(t, \omega) \mathbf{V}^\lambda(\omega)] \Big|_0^T \\ \therefore \langle\langle J_{11}^\lambda \rangle\rangle &= 0. \end{aligned} \quad (\text{C33})$$

Afterwards the second part (II) can be written as

$$\begin{aligned} \langle J_{12}^\lambda(t) \rangle &= 2e \int d\omega f^\lambda(\omega) \int_0^\infty d\tau \text{Re} [\text{Tr} [\mathbf{G}^\dagger(t, \omega) e^{i\omega\tau} \mathbf{\Gamma}(\tau) \mathbf{G}(t - \tau, \omega) \mathbf{V}^\lambda(\omega)]], \\ \implies \langle\langle J_{12}^\lambda \rangle\rangle &= \frac{1}{T} \int_0^T dt \langle J_{12}^\lambda(t) \rangle \\ &= 2e \int d\omega f^\lambda(\omega) \sum_k \text{Tr} \left[\mathbf{G}^{(k)\dagger}(\omega) \left(\frac{\mathbf{\Gamma}(\omega + k\Omega) + \mathbf{\Gamma}^\dagger(\omega + k\Omega)}{2} \right) \mathbf{G}^{(k)}(\omega) \mathbf{V}^\lambda(\omega) \right] \\ &= -2\pi e \int d\omega \sum_{k, \lambda'} \text{Tr} \left[\mathbf{G}^{(k)\dagger}(\omega) \left(\mathbf{V}^{\lambda'T}(\omega + k\Omega) \right) \mathbf{G}^{(k)}(\omega) \mathbf{V}^\lambda(\omega) \right] f^\lambda(\omega). \end{aligned}$$

Thus adding the two contributions, we have

$$\begin{aligned} \langle\langle J_1^\lambda \rangle\rangle &= \langle\langle J_{11}^\lambda \rangle\rangle + \langle\langle J_{12}^\lambda \rangle\rangle \\ &= -2\pi e \int d\omega \sum_{k, \lambda'} \text{Tr} \left[\mathbf{G}^{(k)\dagger}(\omega) \left(\mathbf{V}^{\lambda'T}(\omega + k\Omega) \right) \mathbf{G}^{(k)}(\omega) \mathbf{V}^\lambda(\omega) \right] f^\lambda(\omega). \end{aligned} \quad (\text{C34})$$

Similarly, we can have (from the second term of Eq. (C29), $\langle J_2^\lambda(t) \rangle$)

$$\langle\langle J_2^\lambda \rangle\rangle = 2\pi e \int d\omega \sum_{k, \lambda'} \text{Tr} \left[\mathbf{G}^{(k)\dagger}(\omega) \left(\mathbf{V}^{\lambda T}(\omega + k\Omega) \right) \mathbf{G}^{(k)}(\omega) \mathbf{V}^{\lambda'}(\omega) \right] f^{\lambda'}(\omega). \quad (\text{C35})$$

Therefore, the average current through the λ^{th} lead over

a full time period is given by

$$\begin{aligned} \langle\langle J^\lambda \rangle\rangle &= \langle\langle J_1^\lambda \rangle\rangle + \langle\langle J_2^\lambda \rangle\rangle \\ &= 2\pi e \int d\omega \sum_k \left(\mathbf{T}_{\lambda\lambda'}^{(k)} f^{\lambda'}(\omega) - \mathbf{T}_{\lambda'\lambda}^{(k)} f^\lambda(\omega) \right), \end{aligned} \quad (\text{C36})$$

where, the dynamical equivalence of transmission probability is defined as

$$\mathbf{T}_{\lambda\lambda'}^{(k)}(\omega) = \text{Tr} \left[\mathbf{G}^{(k)\dagger}(\omega) (\mathbf{V}^{\lambda T}(\omega + k\Omega)) \mathbf{G}^{(k)}(\omega) \mathbf{V}^{\lambda'}(\omega) \right]. \quad (\text{C37})$$

Considering a two terminal setup ($\lambda = L$, and $\lambda' = L, R$), we have total current through the left lead as

$$\begin{aligned} \langle\langle J^L \rangle\rangle &= 2\pi e \int d\omega \sum_k \left[\mathbf{T}_{LR}^{(k)} f^R(\omega) - \mathbf{T}_{RL}^{(k)} f^L(\omega) \right] \\ &= 2\pi e \int d\omega \sum_k \mathbf{T}_{LL}^{(k)} [1 - f^L(\omega) - f^R(-\omega)] \\ &\quad + 2\pi e \int d\omega \sum_k \left[\mathbf{T}_{LR}^{(k)} f^R(\omega) - \mathbf{T}_{RL}^{(k)} f^L(\omega) \right] \end{aligned} \quad (\text{C38})$$

If the applied bias at the two leads L and R are $\pm V/2$, then the differential conductance at the left lead is given by

$$\begin{aligned} \sigma^L(V) &= e \frac{d\langle\langle J^L \rangle\rangle}{d\mu} \\ &= -2\pi e^2 \int d\omega \sum_k \mathbf{T}_{LL}^{(k)} [f'^L(\omega) + f'^R(-\omega)] \\ &\quad + 2\pi e^2 \int d\omega \sum_k \left[\mathbf{T}_{LR}^{(k)} f'^R(\omega) - \mathbf{T}_{RL}^{(k)} f'^L(\omega) \right]. \end{aligned} \quad (\text{C39})$$

In flat band limit, lead density of states can be approximated as $\rho(\omega + k\Omega) \approx \rho = \text{constant}$ i.e., $\mathbf{V}(\omega) \approx \mathbf{V}$. Using the above equation, and implementing non-equilibrium Green's function (NEGF) technique, one can calculate differential conductance numerically. However, for one terminal setup (single lead contact), we can proceed further with an analytical approach. For single terminal setup, there is no right lead and the conductance becomes

$$\begin{aligned} \sigma(V) &= -2\pi e^2 \mathbf{T}_{LL}^{(k)} f'^L(\omega) \\ &= -2\pi e^2 \int d\omega \sum_k \text{Tr} \left[\mathbf{G}^{(k)\dagger}(\omega) \mathbf{V}^T \mathbf{G}^{(k)}(\omega) \mathbf{V} \right] f'(\omega). \end{aligned} \quad (\text{C40})$$

For one terminal setup and weak coupling limit ($\nu \ll t_h$), the coupling matrix \mathbf{K} vanishes except at the contact point i.e. $\mathbf{K} = \mathbf{K}^c \oplus 0 \oplus 0 \oplus \dots N$ times, with N being the system size. Consequently, $\mathbf{V} = \mathbf{V}^c \oplus 0 \oplus 0 \oplus \dots N$ times. Therefore, the coupling term at the contact site in electronic basis becomes $t_h a^{c\dagger} c^c$ (superscript $c \implies$ contact) with t_h being the hopping amplitude. We know the basis transformation between electronic and Majorana basis which is given by: $a^c/c^c = (1/\sqrt{2})(\gamma_{a_1/c_1} + i\gamma_{a_2/c_2})$. Thus the coupling term is given by

$$\begin{aligned} &\frac{t_h}{2} (\gamma_{a_1} - i\gamma_{a_2})(\gamma_{c_1} + i\gamma_{c_2}) \\ &= \frac{t_h}{2} (\gamma_{a_1} \ \gamma_{a_2}) \begin{pmatrix} 1 & i \\ -i & 1 \end{pmatrix} \begin{pmatrix} \gamma_{c_1} \\ \gamma_{c_2} \end{pmatrix}. \end{aligned} \quad (\text{C41})$$

In Majorana basis, at the contact site coupling matrix \mathbf{K}^c is given by $\frac{t_h}{2} \begin{pmatrix} 1 & i \\ -i & 1 \end{pmatrix}$. Then \mathbf{V}^c is given by

$$\begin{aligned} \mathbf{V}^c &= \mathbf{K}^{c\dagger} \rho \mathbf{K}^c \\ &= \rho t_h^2 \frac{1}{2} \begin{pmatrix} 1 & i \\ -i & 1 \end{pmatrix}. \end{aligned}$$

Let us define a new quantity: $\nu = 2\pi\rho t_h^2$. Hence, in Majorana basis, \mathbf{V}^c is given by

$$\mathbf{V}^c = \frac{\nu}{2\pi} \frac{1}{2} (\mathbf{I}_2 - \sigma_y). \quad (\text{C42})$$

For Rashba NW model [75] or Shiba chain model [76], one has to consider spin/chiral degrees of freedom in addition to electron-hole degrees of freedom. Thus, in those cases, the \mathbf{V}^c matrix can be written in the form

$$\mathbf{V}^c = \rho t_h^2 \frac{1}{2} \begin{pmatrix} 1 & i \\ -i & 1 \end{pmatrix} \otimes \begin{pmatrix} 1 & 0 \\ 0 & 1 \end{pmatrix}. \quad (\text{C43})$$

Using this relation in Eq. (C40) we have

$$\sigma(V) = -\frac{e^2 \nu^2}{2\pi} \times 2 \times \sum_{k,s,s'} \int d\omega |G_{he,ss'}^{c(k)}(\omega)|^2 f'(\omega), \quad (\text{C44})$$

where, $G_{he,ss'}^{c(k)}$ corresponds to the hole (with spin/chirality)-electron (with s' -spin/chirality) component of Nambu-Gorkov Green's function for photon sector k computed at the contact site. In the weak coupling limit, one can carry out perturbative analysis at the contact point to obtain the self-energy following [81] as

$$\begin{aligned} \delta_{\bar{\alpha}} &= -\langle\langle -\pi (\mathbf{V} + \mathbf{V}^T) \rangle\rangle \\ &= \frac{\nu}{2} \sum_k \langle u_{\bar{\alpha}}^{c(k)} | \mathbf{I}_4 | u_{\bar{\alpha}}^{c(k)} \rangle \\ &= \frac{\nu}{2} \sum_{k,s} \left[|u_{\bar{\alpha},s}^{c(k)}|^2 + |v_{\bar{\alpha},s}^{c(k)}|^2 \right], \end{aligned} \quad (\text{C45})$$

where $u_{\bar{\alpha},s}^{c(k)}$, and $v_{\bar{\alpha},s}^{c(k)}$ are particle and hole components of the wave function, respectively, for spin/chiral sector s and photon sector k at the contact site. Therefore, in the zero temperature limit, one terminal differential

conductance in presence of a bias voltage V is given by

$$\begin{aligned}
\tilde{\sigma}(V) &= \lim_{V \rightarrow \epsilon_{\bar{\alpha}}} \frac{e^2 \nu^2}{2\pi} \times 2 \sum_{k,s,s'} |G_{he,ss'}^{c(k)}(V + n\Omega)|^2 \\
&= \frac{e^2 \nu^2}{2\pi} \times 2 \sum_{n,k,s,s',\bar{\alpha}} \left| \frac{|u_{\bar{\alpha}}^{(n+k)}\rangle \langle u_{\bar{\alpha}}^{+(n)}|}{V - \epsilon_{\bar{\alpha}} + i\delta_{\bar{\alpha}}} \right|_{he,ss'}^c \Big|^2 \\
&\approx \frac{e^2 \nu^2}{2\pi} \times 2 \sum_{n,k,s,s',\bar{\alpha}} \left| \frac{v_{\bar{\alpha},s}^{c(k+n)} u_{\bar{\alpha},s'}^{c(n)}}{V - \epsilon_{\bar{\alpha}} + i\delta_{\bar{\alpha}}} \right|^2 \\
&= \frac{e^2 \nu^2}{2\pi} \times 2 \sum_{n,k,s,s',\bar{\alpha}} \frac{|v_{\bar{\alpha},s}^{c(k+n)} u_{\bar{\alpha},s'}^{c(n)}|^2}{|V - \epsilon_{\bar{\alpha}} + i\delta_{\bar{\alpha}}|^2} \\
&= \frac{2e^2}{h} \times \sum_{n,\bar{\alpha},k,s,s'} \frac{\nu^2}{\delta_{\bar{\alpha}}^2} \times \frac{|v_{\bar{\alpha},s}^{c(k+n)} u_{\bar{\alpha},s'}^{c(n)}|^2}{\left(\frac{V - \epsilon_{\bar{\alpha}}}{\delta_{\bar{\alpha}}}\right)^2 + 1} \\
&= \sum_n \frac{2e^2}{h} \sum_{\bar{\alpha},k,s,s'} \frac{\nu^2}{\delta_{\bar{\alpha}}^2} \times |v_{\bar{\alpha},s}^{c(k+n)} u_{\bar{\alpha},s'}^{c(n)}|^2 \times L\left(\frac{V - \epsilon_{\bar{\alpha}}}{\delta_{\bar{\alpha}}}\right) \\
&= \sum_n \sigma(V + n\Omega), \tag{C46}
\end{aligned}$$

with $\sigma(V + n\Omega) = \frac{2e^2}{h} \sum_{\bar{\alpha},k,s,s'} \frac{\nu^2}{\delta_{\bar{\alpha}}^2} \times |v_{\bar{\alpha},s}^{c(k+n)} u_{\bar{\alpha},s'}^{c(n)}|^2 \times L\left(\frac{V - \epsilon_{\bar{\alpha}}}{\delta_{\bar{\alpha}}}\right) \equiv \sigma^{(n)}(V)$. Here, the Lorentzian is defined by $L(z) = \frac{1}{1+z^2}$.

Appendix D: Extended (frequency) space Hamiltonian

In order to calculate $\tilde{\sigma}$, we need the Floquet states in frequency space $|u_{\bar{\alpha}}^{(n)}\rangle$ and its components at contact sites. In this regard we diagonalize the extended space Hamiltonian following the reference [84]. The extended space Hamiltonian has the form:

$$\begin{pmatrix}
\ddots & \vdots & \vdots & \vdots & \vdots & \vdots & \ddots \\
\cdots & H^{(0)} - 2\Omega & H^{(-1)} & H^{(-2)} & H^{(-3)} & H^{(-4)} & \cdots \\
\cdots & H^{(1)} & H^{(0)} - \Omega & H^{(-1)} & H^{(-2)} & H^{(-3)} & \cdots \\
\cdots & H^{(2)} & H^{(1)} & H^{(0)} & H^{(-1)} & H^{(-2)} & \cdots \\
\cdots & H^{(3)} & H^{(2)} & H^{(1)} & H^{(0)} + \Omega & H^{(-1)} & \cdots \\
\cdots & H^{(4)} & H^{(3)} & H^{(2)} & H^{(1)} & H^{(0)} + 2\Omega & \cdots \\
\ddots & \vdots & \vdots & \vdots & \vdots & \vdots & \ddots
\end{pmatrix}$$

having block dimension $4N \times 4N$ with $H^{(n)} = \int_0^T \frac{dt}{T} e^{in\Omega t} H(t) = H^{(-n)\dagger}$. The form of these blocks depend on the nature of the external drive. We calculate the same for both of our driving protocols as mentioned for Rashba NW and helical Shiba chain.

1. Three step drive protocol

For the step drive protocol introduced in Rasha NW case [Eq. (2) in the main text], the block $H^{(0)}$ in the diagonal is given by $\frac{1}{2}[H_1 + H_0]$. However, off-diagonal blocks carry the form

$$H^{(n)} = \frac{(e^{\frac{in\pi}{2}} - e^{\frac{in3\pi}{2}})}{i2\pi n} [H_1 - H_0]. \tag{D2}$$

Non-zero even values of n yield $H^{(n=\text{even})} = 0$. However, for odd n , we have $H^{(\pm 1)} = \frac{1}{\pi}[H_1 - H_0]$, $H^{(\pm 3)} = -\frac{1}{3\pi}[H_1 - H_0]$, $H^{(\pm 5)} = \frac{1}{5\pi}[H_1 - H_0]$,.....etc. Note that, $H^{(n)}$ exhibits a $1/n$ fall.

2. Sinusoidal drive protocol

In case of sinusoidal drive applied in Helical Shiba chain (magnet-superconductor hybrid structure) [Eq. (14) in the main text], the block in diagonal $H^{(0)}$ represents the static Hamiltonian H_0 itself. Also, only remaining non-vanishing off-diagonal blocks are $H^{(\pm 1)}$ which are given by $H^{(\pm 1)} = \frac{V_0}{2} \mathbf{I}_N \otimes \Gamma_1$.

Although the extended space Hamiltonian has infinite number of blocks, one can truncate the blocks for large n as they do not effectively contribute to the emergent quasi-energies. For our numerical computations, we consider $n = -10$ to $n = 10$ i.e., total $2 \times 10 + 1 = 21$ photon sectors. Therefore, we effectively diagonalize $84N \times 84N$ ($21 \times N \times 4 = 84N$) matrix to obtain quasi-energies $\epsilon_{\bar{\alpha}}$ and quasi-states $|u_{\bar{\alpha}}^{(n)}\rangle$.

Appendix E: Transport signature of static MZMs in Rashba NW for small system size

Here, we repeat the transport signature of static MZMs in Rashba NW model considering small system size. We consider a system size of $N = 100$ lattice sites and obtain corresponding two Majorana wave functions exhibiting full overlap between themselves resulting in the quantized value of $2 \times 2e^2/h = 4e^2/h$ for the ZBP height in case of static one terminal conductance σ_{stat} . This is depicted in Fig. 11. We show this in order to convey that even for the static case, if one cannot resolve the Majorana wave functions at the two ends of the system (for small system size in general), the ZBP height would be $2 \times 2e^2/h = 4e^2/h$.

(D1) Appendix F: Transport signature of edge-resolved FMEMs in Rashba NW

Here, we recapitulate case 2 (only one π -FMEM as described in the main text of Sec. IV B). Therefore, we carry out transport study for single π -FMEM considering large system size. We obtain the corresponding wave functions

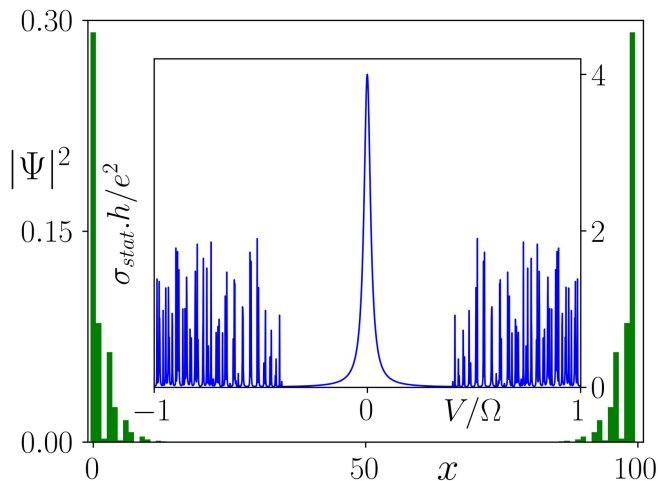


FIG. 11. We reinvestigate Fig. 2 of the main text considering small system size ($N = 100$). Note that, the wave functions are not edge-resolved in this case and we obtain $4e^2/h$ quantization for σ_{stat} at $V = 0$ (see the inset ZBP). All the other model parameters are chosen to be the same as mentioned in Fig. 2.

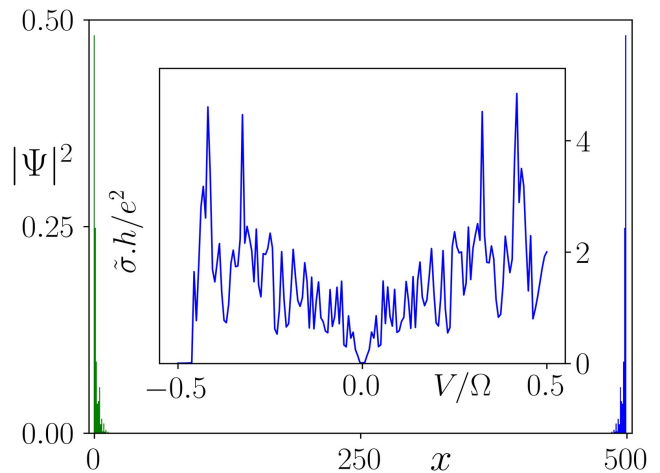


FIG. 12. We repeat Fig. 4(b) considering large system size ($N = 500$). The Floquet Majorana wave functions become edge-resolved as shown by the probability density $|\Psi|^2$ in terms of the system size. Thus, we obtain $2e^2/h$ quantization for $\bar{\sigma}$ at $V = \Omega/2$ having contribution from one π -mode wave function (see the inset). All the other model parameters remain same as mentioned in Fig. 4(b).

to be edge-resolved (see Fig. 12) in this case and summed conductance $\bar{\sigma}$ exhibits $2e^2/h$ quantization at $V = \Omega/2$. However, we are unable to obtain edge-resolved Floquet Majorana wave functions for the other cases considering suitable system sizes within our numerical computation facility.

-
- [1] A. Y. Kitaev, “Unpaired majorana fermions in quantum wires,” *Physics-Uspekhi* **44**, 131–136 (2001).
- [2] X.-L. Qi and S.-C. Zhang, “Topological insulators and superconductors,” *Rev. Mod. Phys.* **83**, 1057 (2011).
- [3] M. Leijnse and K. Flensberg, “Introduction to topological superconductivity and majorana fermions,” *Semiconductor Science and Technology* **27**, 124003 (2012).
- [4] J. Alicea, “New directions in the pursuit of majorana fermions in solid state systems,” *Reports on Progress in Physics* **75**, 076501 (2012).
- [5] R. Aguado, “Majorana quasiparticles in condensed matter,” *Riv. Nuovo Cimento* **40**, 523 (2017).
- [6] C. Beenakker, “Search for majorana fermions in superconductors,” *Annu. Rev. Condens. Matter Phys.* **4**, 113–136 (2013).
- [7] D. A. Ivanov, “Non-abelian statistics of half-quantum vortices in p -wave superconductors,” *Phys. Rev. Lett.* **86**, 268–271 (2001).
- [8] M. Freedman, A. Kitaev, M. Larsen, and Z. Wang, “Topological quantum computation,” *Bulletin of the American Mathematical Society* **40**, 31–38 (2003).
- [9] A. Kitaev, “Fault-tolerant quantum computation by anyons,” *Annals of Physics* **303**, 2–30 (2003).
- [10] A. Stern, “Non-abelian states of matter,” *Nature* **464**, 187–193 (2010).
- [11] C. Nayak, S. H. Simon, A. Stern, M. Freedman, and S. Das Sarma, “Non-abelian anyons and topological quantum computation,” *Rev. Mod. Phys.* **80**, 1083–1159 (2008).
- [12] Y. Oreg, G. Refael, and F. von Oppen, “Helical liquids and majorana bound states in quantum wires,” *Phys. Rev. Lett.* **105**, 177002 (2010).
- [13] R. M. Lutchyn, J. D. Sau, and S. Das Sarma, “Majorana fermions and a topological phase transition in semiconductor-superconductor heterostructures,” *Phys. Rev. Lett.* **105**, 077001 (2010).
- [14] V. Mourik, K. Zuo, S. M. Frolov, S. R. Plissard, E. P. A. M. Bakkers, and L. P. Kouwenhoven, “Signatures of majorana fermions in hybrid superconductor-semiconductor nanowire devices,” *Science* **336**, 1003–1007 (2012).
- [15] A. Das, Y. Ronen, Y. Most, Y. Oreg, M. Heiblum, and H. Shtrikman, “Zero-bias peaks and splitting in an al-inas nanowire topological superconductor as a signature of majorana fermions,” *Nature Physics* **8**, 887–895 (2012).
- [16] L. P. Rokhinson, X. Liu, and J. K. Furdyna, “The fractional a.c. josephson effect in a semiconductor-superconductor nanowire as a signature of majorana particles,” *Nature Physics* **8**, 795–799 (2012).

- [17] A. D. K. Finck, D. J. Van Harlingen, P. K. Mohseni, K. Jung, and X. Li, “Anomalous modulation of a zero-bias peak in a hybrid nanowire-superconductor device,” *Phys. Rev. Lett.* **110**, 126406 (2013).
- [18] S. M. Albrecht, A. P. Higginbotham, M. Madsen, F. Kuemmeth, T. S. Jespersen, J. Nygård, P. Krogstrup, and C. M. Marcus, “Exponential protection of zero modes in majorana islands,” *Nature* **531**, 206–209 (2016).
- [19] M. T. Deng, S. Vaitiekėnas, E. B. Hansen, J. Danon, M. Leijnse, K. Flensberg, J. Nygård, P. Krogstrup, and C. M. Marcus, “Majorana bound state in a coupled quantum-dot hybrid-nanowire system,” *Science* **354**, 1557–1562 (2016).
- [20] S. Nadj-Perge, I. K. Drozdov, B. A. Bernevig, and A. Yazdani, “Proposal for realizing majorana fermions in chains of magnetic atoms on a superconductor,” *Phys. Rev. B* **88**, 020407 (2013).
- [21] F. Pientka, L. I. Glazman, and F. von Oppen, “Topological superconducting phase in helical shiba chains,” *Phys. Rev. B* **88**, 155420 (2013).
- [22] J. Klinovaja, P. Stano, A. Yazdani, and D. Loss, “Topological superconductivity and majorana fermions in rkk systems,” *Phys. Rev. Lett.* **111**, 186805 (2013).
- [23] F. Pientka, L. I. Glazman, and F. von Oppen, “Unconventional topological phase transitions in helical shiba chains,” *Phys. Rev. B* **89**, 180505 (2014).
- [24] K. Pöyhönen, A. Westström, J. Röntynen, and T. Ojanen, “Majorana states in helical shiba chains and ladders,” *Phys. Rev. B* **89**, 115109 (2014).
- [25] N. Sedlmayr, J. M. Aguiar-Hualde, and C. Bena, “Flat majorana bands in two-dimensional lattices with inhomogeneous magnetic fields: Topology and stability,” *Phys. Rev. B* **91**, 115415 (2015).
- [26] S. Hoffman, J. Klinovaja, and D. Loss, “Topological phases of inhomogeneous superconductivity,” *Phys. Rev. B* **93**, 165418 (2016).
- [27] M. H. Christensen, M. Schechter, K. Flensberg, B. M. Andersen, and J. Paaske, “Spiral magnetic order and topological superconductivity in a chain of magnetic adatoms on a two-dimensional superconductor,” *Phys. Rev. B* **94**, 144509 (2016).
- [28] G. M. Andolina and P. Simon, “Topological properties of chains of magnetic impurities on a superconducting substrate: Interplay between the shiba band and ferromagnetic wire limits,” *Phys. Rev. B* **96**, 235411 (2017).
- [29] D. Sticlet and C. Morari, “Topological superconductivity from magnetic impurities on monolayer nbse₂,” *Phys. Rev. B* **100**, 075420 (2019).
- [30] S. Rex, I. V. Gornyi, and A. D. Mirlin, “Majorana modes in emergent-wire phases of helical and cycloidal magnet-superconductor hybrids,” *Phys. Rev. B* **102**, 224501 (2020).
- [31] N. Mohanta, S. Okamoto, and E. Dagotto, “Skyrmion control of majorana states in planar josephson junctions,” *Communications Physics* **4**, 163 (2021).
- [32] R. Hess, H. F. Legg, D. Loss, and J. Klinovaja, “Prevalence of trivial zero-energy subgap states in nonuniform helical spin chains on the surface of superconductors,” *Phys. Rev. B* **106**, 104503 (2022).
- [33] P. Chatterjee, S. Pradhan, A. K. Nandy, and A. Saha, “Tailoring the phase transition from topological superconductor to trivial superconductor induced by magnetic textures of a spin chain on a p -wave superconductor,” *Phys. Rev. B* **107**, 085423 (2023).
- [34] J. D. Sau and E. Demler, “Bound states at impurities as a probe of topological superconductivity in nanowires,” *Phys. Rev. B* **88**, 205402 (2013).
- [35] S. Nakosai, Y. Tanaka, and N. Nagaosa, “Two-dimensional p -wave superconducting states with magnetic moments on a conventional s -wave superconductor,” *Phys. Rev. B* **88**, 180503 (2013).
- [36] H.-Y. Hui, P. M. R. Brydon, J. D. Sau, S. Tewari, and S. D. Sarma, “Majorana fermions in ferromagnetic chains on the surface of bulk spin-orbit coupled s -wave superconductors,” *Scientific Reports* **5**, 8880 (2015).
- [37] J. Röntynen and T. Ojanen, “Topological superconductivity and high chern numbers in 2d ferromagnetic shiba lattices,” *Phys. Rev. Lett.* **114**, 236803 (2015).
- [38] G. Sharma and S. Tewari, “Yu-shiba-rusinov states and topological superconductivity in ising paired superconductors,” *Phys. Rev. B* **94**, 094515 (2016).
- [39] A. Theiler, K. Björnson, and A. M. Black-Schaffer, “Majorana bound state localization and energy oscillations for magnetic impurity chains on conventional superconductors,” *Phys. Rev. B* **100**, 214504 (2019).
- [40] M. Mashkooi, S. Pradhan, K. Björnson, J. Fransson, and A. M. Black-Schaffer, “Identification of topological superconductivity in magnetic impurity systems using bulk spin polarization,” *Phys. Rev. B* **102**, 104501 (2020).
- [41] R. L. R. C. Teixeira, D. Kuzmanovski, A. M. Black-Schaffer, and L. G. G. V. D. da Silva, “Enhanced majorana bound states in magnetic chains on superconducting topological insulator edges,” *Phys. Rev. B* **102**, 165312 (2020).
- [42] S. Nadj-Perge, I. K. Drozdov, J. Li, H. Chen, S. Jeon, J. Seo, A. H. MacDonald, B. A. Bernevig, and A. Yazdani, “Observation of majorana fermions in ferromagnetic atomic chains on a superconductor,” *Science* **346**, 602–607 (2014).
- [43] A. Yazdani, “Visualizing majorana fermions in a chain of magnetic atoms on a superconductor,” *Physica Scripta* **2015**, 014012 (2015).
- [44] H. Kim, A. Palacio-Morales, T. Posske, L. Rózsa, K. Palotás, L. Szunyogh, M. Thorwart, and R. Wiesendanger, “Toward tailoring majorana bound states in artificially constructed magnetic atom chains on elemental superconductors,” *Science Advances* **4**, eaar5251 (2018).
- [45] L. Schneider, S. Brinker, M. Steinbrecher, J. Hermenau, T. Posske, M. dos Santos Dias, S. Lounis, R. Wiesendanger, and J. Wiebe, “Controlling in-gap end states by linking nonmagnetic atoms and artificially-constructed spin chains on superconductors,” *Nature Communications* **11**, 4707 (2020).
- [46] L. Schneider, P. Beck, T. Posske, D. Crawford, E. Mascot, S. Rachel, R. Wiesendanger, and J. Wiebe, “Topological shiba bands in artificial spin chains on superconductors,” *Nature Physics* **17**, 943–948 (2021).
- [47] P. Beck, L. Schneider, L. Rózsa, K. Palotás, A. Lászlóffy, L. Szunyogh, J. Wiebe, and R. Wiesendanger, “Spin-orbit coupling induced splitting of yu-shiba-rusinov states in antiferromagnetic dimers,” *Nature Communications* **12**, 2040 (2021).
- [48] D. Wang, J. Wiebe, R. Zhong, G. Gu, and R. Wiesendanger, “Spin-polarized yu-shiba-rusinov states in an iron-based superconductor,” *Phys. Rev. Lett.* **126**, 076802 (2021).

- [49] L. Schneider, P. Beck, J. Neuhaus-Steinmetz, L. Rózsa, T. Posske, J. Wiebe, and R. Wiesendanger, “Precursors of majorana modes and their length-dependent energy oscillations probed at both ends of atomic shiba chains,” *Nature Nanotechnology* **17**, 384–389 (2022).
- [50] D. Crawford, E. Mascot, M. Shimizu, P. Beck, J. Wiebe, R. Wiesendanger, H. O. Jeschke, D. K. Morr, and S. Rachel, “Majorana modes with side features in magnet-superconductor hybrid systems,” *npj Quantum Materials* **7**, 117 (2022).
- [51] T. Oka and H. Aoki, “Photovoltaic hall effect in graphene,” *Phys. Rev. B* **79**, 081406 (2009).
- [52] T. Kitagawa, T. Oka, A. Brataas, L. Fu, and E. Demler, “Transport properties of nonequilibrium systems under the application of light: Photoinduced quantum hall insulators without landau levels,” *Phys. Rev. B* **84**, 235108 (2011).
- [53] N. H. Lindner, G. Refael, and V. Galitski, “Floquet topological insulator in semiconductor quantum wells,” *Nature Phys* **7**, 490–495 (2011).
- [54] M. S. Rudner, N. H. Lindner, E. Berg, and M. Levin, “Anomalous edge states and the bulk-edge correspondence for periodically driven two-dimensional systems,” *Phys. Rev. X* **3**, 031005 (2013).
- [55] G. Usaj, P. M. Perez-Piskunow, L. E. F. Foa Torres, and C. A. Balseiro, “Irradiated graphene as a tunable floquet topological insulator,” *Phys. Rev. B* **90**, 115423 (2014).
- [56] P. M. Perez-Piskunow, G. Usaj, C. A. Balseiro, and L. E. F. F. Torres, “Floquet chiral edge states in graphene,” *Phys. Rev. B* **89**, 121401 (2014).
- [57] A. Eckardt, “Colloquium: Atomic quantum gases in periodically driven optical lattices,” *Rev. Mod. Phys.* **89**, 011004 (2017).
- [58] S. Yao, Z. Yan, and Z. Wang, “Topological invariants of floquet systems: General formulation, special properties, and floquet topological defects,” *Phys. Rev. B* **96**, 195303 (2017).
- [59] T. Oka and S. Kitamura, “Floquet engineering of quantum materials,” *Annual Review of Condensed Matter Physics* **10**, 387–408 (2019).
- [60] M. Rudner and N. Lindner, “Band structure engineering and non-equilibrium dynamics in floquet topological insulators,” *Nat. Rev. Phys.* **2**, 229–244 (2020).
- [61] T. Nag and B. Roy, “Anomalous and normal dislocation modes in floquet topological insulators,” *Commun Phys* **4**, 157 (2021).
- [62] M. Thakurathi, A. A. Patel, D. Sen, and A. Dutta, “Floquet generation of majorana end modes and topological invariants,” *Phys. Rev. B* **88**, 155133 (2013).
- [63] M. Benito, A. Gómez-León, V. M. Bastidas, T. Brandes, and G. Platero, “Floquet engineering of long-range p -wave superconductivity,” *Phys. Rev. B* **90**, 205127 (2014).
- [64] A. C. Potter, T. Morimoto, and A. Vishwanath, “Classification of interacting topological floquet phases in one dimension,” *Phys. Rev. X* **6**, 041001 (2016).
- [65] L. Jiang, T. Kitagawa, J. Alicea, A. R. Akhmerov, D. Pekker, G. Refael, J. I. Cirac, E. Demler, M. D. Lukin, and P. Zoller, “Majorana fermions in equilibrium and in driven cold-atom quantum wires,” *Phys. Rev. Lett.* **106**, 220402 (2011).
- [66] A. A. Reynoso and D. Frustaglia, “Unpaired floquet majorana fermions without magnetic fields,” *Phys. Rev. B* **87**, 115420 (2013).
- [67] D. E. Liu, A. Levchenko, and H. U. Baranger, “Floquet majorana fermions for topological qubits in superconducting devices and cold-atom systems,” *Phys. Rev. Lett.* **111**, 047002 (2013).
- [68] M. Thakurathi, D. Loss, and J. Klinovaja, “Floquet majorana fermions and parafermions in driven rashba nanowires,” *Phys. Rev. B* **95**, 155407 (2017).
- [69] D. T. Liu, J. Shabani, and A. Mitra, “Floquet majorana zero and π modes in planar josephson junctions,” *Phys. Rev. B* **99**, 094303 (2019).
- [70] Z. Yang, Q. Yang, J. Hu, and D. E. Liu, “Dissipative floquet majorana modes in proximity-induced topological superconductors,” *Phys. Rev. Lett.* **126**, 086801 (2021).
- [71] P. D. Sacramento, “Charge and spin edge currents in two-dimensional floquet topological superconductors,” *Phys. Rev. B* **91**, 214518 (2015).
- [72] R.-X. Zhang and S. Das Sarma, “Anomalous floquet chiral topological superconductivity in a topological insulator sandwich structure,” *Phys. Rev. Lett.* **127**, 067001 (2021).
- [73] D. M. Kennes, N. Müller, M. Pletyukhov, C. Weber, C. Bruder, F. Hassler, J. Klinovaja, D. Loss, and H. Schoeller, “Chiral one-dimensional floquet topological insulators beyond the rotating wave approximation,” *Phys. Rev. B* **100**, 041103 (2019).
- [74] N. Müller, D. M. Kennes, J. Klinovaja, D. Loss, and H. Schoeller, “Electronic transport in one-dimensional floquet topological insulators via topological and non-topological edge states,” *Phys. Rev. B* **101**, 155417 (2020).
- [75] D. Mondal, A. K. Ghosh, T. Nag, and A. Saha, “Topological characterization and stability of floquet majorana modes in rashba nanowires,” *Phys. Rev. B* **107**, 035427 (2023).
- [76] D. Mondal, A. K. Ghosh, T. Nag, and A. Saha, “Engineering anomalous floquet majorana modes and their time evolution in a helical shiba chain,” *Phys. Rev. B* **108**, L081403 (2023).
- [77] R. W. Bomantara and J. Gong, “Simulation of non-abelian braiding in majorana time crystals,” *Phys. Rev. Lett.* **120**, 230405 (2018).
- [78] R. W. Bomantara and J. Gong, “Quantum computation via floquet topological edge modes,” *Phys. Rev. B* **98**, 165421 (2018).
- [79] B. Bauer, T. Pereg-Barnea, T. Karzig, M.-T. Rieder, G. Refael, E. Berg, and Y. Oreg, “Topologically protected braiding in a single wire using floquet majorana modes,” *Phys. Rev. B* **100**, 041102 (2019).
- [80] A. Matthies, J. Park, E. Berg, and A. Rosch, “Stability of floquet majorana box qubits,” *Phys. Rev. Lett.* **128**, 127702 (2022).
- [81] A. Kundu and B. Seradjeh, “Transport signatures of floquet majorana fermions in driven topological superconductors,” *Phys. Rev. Lett.* **111**, 136402 (2013).
- [82] A. Farrell and T. Pereg-Barnea, “Photon-inhibited topological transport in quantum well heterostructures,” *Phys. Rev. Lett.* **115**, 106403 (2015).
- [83] A. Farrell and T. Pereg-Barnea, “Edge-state transport in floquet topological insulators,” *Phys. Rev. B* **93**, 045121 (2016).
- [84] A. Eckardt and E. Anisimovas, “High-frequency approximation for periodically driven quantum systems from a floquet-space perspective,” *New Journal of Physics* **17**, 093039 (2015).

- [85] M. Rodriguez-Vega, M. Lentz, and B. Seradjeh, “Floquet perturbation theory: formalism and application to low-frequency limit,” *New Journal of Physics* **20**, 093022 (2018).
- [86] M. Misiorny, G. Fève, and J. Splettstoesser, “Shaping charge excitations in chiral edge states with a time-dependent gate voltage,” *Phys. Rev. B* **97**, 075426 (2018).
- [87] E. Khosravi, G. Stefanucci, S. Kurth, and E. Gross, “Bound states in time-dependent quantum transport: oscillations and memory effects in current and density,” *Phys. Chem. Chem. Phys.* **11**, 4535–4538 (2009).
- [88] J. Dubois, T. Jullien, F. Portier, P. Roche, A. Cavanna, Y. Jin, W. Wegscheider, P. Roulleau, and D. Glatli, “Minimal-excitation states for electron quantum optics using levitons,” *Nature* **502**, 659–663 (2013).
- [89] J. Gabelli and B. Reulet, “Shaping a time-dependent excitation to minimize the shot noise in a tunnel junction,” *Phys. Rev. B* **87**, 075403 (2013).
- [90] L. Schneider, P. Beck, T. Posske, D. Crawford, E. Mascot, S. Rachel, R. Wiesendanger, and J. Wiebe, “Topological shiba bands in artificial spin chains on superconductors,” *Nature Physics* **17**, 943–948 (2021).
- [91] D. M. Eigler and E. K. Schweizer, “Positioning single atoms with a scanning tunnelling microscope,” *Nature* **344**, 524–526 (1990).
- [92] S. Kohler, J. Lehmann, and P. Hänggi, “Driven quantum transport on the nanoscale,” *Physics Reports* **406**, 379–443 (2005).